ICEBERG PROPERTIES AND DISTRIBUTIONS IN THREE GREENLANDIC FJORDS USING SATELLITE IMAGERY

by

DANIEL J SULAK

A THESIS

Presented to the Department of Geological Sciences
and the Graduate School of the University of Oregon
in partial fulfillment of the requirements
for the degree of
Master of Science

September 2016

THESIS APPROVAL PAGE

Student: Daniel J. Sulak

Title: Iceberg Properties and Distributions in Three Greenlandic Fjords Using Satellite Imagery

This thesis has been accepted and approved in partial fulfillment of the requirements for the Master of Science degree in the Department of Geological Sciences by:

David Sutherland	Chairperson
Josh Roering	Member
Leif Karlstrom	Member

and

Scott L. Pratt	Dean of the Graduate School

Original approval signatures are on file with the University of Oregon Graduate School.

Degree awarded September 2016

THESIS ABSTRACT

Daniel J Sulak

Master of Science

Department of Geological Sciences

September 2016

Title: Iceberg Properties and Distributions in Three Greenlandic Fjords Using Satellite Imagery

Icebergs calved from tidewater glaciers represent significant portions of freshwater flux from the Greenland Ice Sheet to the ocean. Using satellite data sets we quantify properties and distributions of icebergs in three fjords with varied properties: Sermilk, Rink Isbræ, and Kangerdlugssûp Sermerssua. Total iceberg volumes in summer in the three fjords average 6.43, 1.69, and 0.19 km^3, respectively, and we calculate cumulative submerged surface areas of iceberg faces to be 213, 55.2, and 7.57 km^2, respectively. We calculate a freshwater flux from iceberg melt of 0.009 – 0.083 $m^3\ d^{-1}$ in Sermilik Fjord, suggesting a strong potential of iceberg melt water to influence water properties. Properties of icebergs and size distributions are influenced by calving style and grounding line depths of parent glaciers. Variations are represented in the coefficients of generalized Pareto distributions which best describe size distributions in the fjords.

This thesis contains unpublished co-authored material.

CURRICULUM VITAE

NAME OF AUTHOR: Daniel J Sulak

GRADUATE AND UNDERGRADUATE SCHOOLS ATTENDED:

University of Oregon, Eugene
University of Hawai‘i, Mānoa
Colorado Mountain College, Steamboat Springs

DEGREES AWARDED:

Master of Science, Geological Sciences, 2016, University of Oregon
Bachelor of Science, Global Environmental Science, 2007, University of Hawai‘i
Associate of Science, 2004, Colorado Mountain College

AREAS OF SPECIAL INTEREST:

Arctic oceanography.
Remote sensing of the environment.

PROFESSIONAL EXPERIENCE:

Biological Technician, US Fish and Wildlife Service, 2011 – 2014

Aquatic Conservation Technician, Colorado Division of Wildlife, 2010

GRANTS, AWARDS, AND HONORS:

Johnston Scholarship, University of Oregon, 2016

Baldwin Scholarship, University of Oregon, 2015

Student Excellence in Research Award, University of Hawai‘i, 2007

Chevron Global Environmental Science Scholarship, University of Hawai‘i, 2005, 2006, 2007

PUBLICATIONS:

Ruttenberg, K.C., & Sulak, D.J. (2011) Sorption and desorption of dissolved organic phosphorus onto iron (oxyhydr)oxides in seawater. *Geochim. Chosmochim. Ac.*, 75(15), 4095-4112.

ACKNOWLEDGMENTS

I would like to express sincere appreciation to my advisor, Professor David Sutherland, for his guidance, insight, and enthusiastic support throughout all stages of this research project. Additionally, gratitude is due to Leigh Stearns, Ellyn Enderlin, and Gordon Hamilton for providing comments and feedback which strengthened the contents of this thesis. I also wish to express thanks to my family, whose unfailing support has enabled my success throughout life's endeavors.

This work was supported in part by grants from NASA (NNX12AP50G) and the National Science Foundation (NSF-PLR 1504521) to Dr. David Sutherland at the University of Oregon, and in part by the state of Oregon.

TABLE OF CONTENTS

Chapter Page

LIST OF FIGURES

Figure Page

LIST OF TABLES

Table Page

CHAPTER I

INTRODUCTION

In response to increasing global temperatures the Greenland Ice Sheet (GrIS) has been undergoing rapid changes including an acceleration of 25.4 Gt yr^{-2} in annual mass loss from 2003 – 2013 (Velicogna et al., 2014). Between 2009 – 2012, mass loss reached 378 Gt yr^{-1}, contributing over 1.0 mm yr^{-1} to global sea level (Enderlin et al., 2014). Ice lost from the GrIS has two components: increased liquid freshwater runoff, and increased calving of icebergs due to widespread acceleration of outlet glaciers (van den Broeke et al., 2009; Moon et al., 2012; Velicogna et al., 2014). Freshwater input from the GrIS to the Irminger Basin increased 50% between 1992 and 2010 (Bamber et al., 2012). This addition can decrease surface water salinity in the North Atlantic, increasing surface buoyancy and potentially affecting the Atlantic Meridional Overturning Circulation (AMOC) by inhibiting convection (Fichefet et al. 2003; Stouffer et al., 2006; Yang et al., 2016).

Between 32% and 50% of the total freshwater discharge from the GrIS is in the form of icebergs calved from tidewater glaciers (Enderlin et al., 2014; van den Broeke et al., 2009). These icebergs can be transported hundreds to thousands of kilometers from their origins (Robe, 1980; Sutherland, et al., 2014; Larsen et al., 2015), releasing sediment as they gradually melt (Dowdeswell & Dowdeswell, 1989; Syvitski et al., 1996; Azetsu-Scott & Syvitski, 1999), providing a source of nutrients (Raiswell et al., 2006), and depositing a record which can be used for paleoclimate reconstructions (Grobe, 1987). Drifting icebergs also present hazards to scientific equipment, off-shore commercial infrastructure such as oil platforms, and ocean-going ships, the most famous

example being the sinking of the Titanic after collision with an iceberg which originated from the GrIS (Bigg & Wilton, 2013). For the above reasons there have been several attempts to model iceberg trajectories and melt (Smith & Donaldson, 1987; Bigg et al., 1996; Bigg & Nicholls, 2001; Death et al., 2006; Mugford & Dowdeswell, 2010). Ocean circulation models are also beginning to incorporate icebergs as a distributed freshwater source (Levine & Bigg, 2008; Martin & Adcroft, 2010).

Accurate observations of iceberg spatial distributions, size distributions, volumes, keel depths, and movement are necessary to quantify the impact of icebergs on seawater properties, interpret sedimentary records, and for the initiation and validation of models. Several studies have focused on icebergs around Antarctica, where iceberg size distributions have been described for limited numbers of medium to large (>100 m length) icebergs observed using radar and sextant (Wadhams, 1988), or by direct visual observation (Neshyba, 1980). Satellite data have also been used to detect icebergs and describe their distributions throughout the Antarctic, though these observations were also limited by the methods of detection to icebergs with lengths greater than 100 m (Neshyba, 1980; Tournadre et al., 2012; Tournadre et al., 2016). These observations are informative, but are for only limited numbers of icebergs, and they are not directly analogous to icebergs in Greenlandic fjords as they focus primarily on large, tabular icebergs calved from Antarctic ice shelves in open ocean rather than in constricted fjords. The number and size range of icebergs observed in the Arctic have been more limited. Distributions and dimensions of limited numbers ($n < 600$) of icebergs, bergy bits (pieces of ice less than 5 m in length), and growlers (pieces less than 2 m in length) have been described (Hotzel & Miller, 1983; Smith & Donaldson, 1987; Crocker, 1993;

Dowdeswell & Forsberg, 1992). Iceberg draughts were detected for 285 icebergs in Sermilik Fjord using an inverted echo sounder (Andres et al., 2015), and sonar profiles of iceberg keels were obtained for nine icebergs near Labrador (Smith & Donaldson, 1987). Enderlin & Hamilton (2014) used stereo satellite imagery to calculate iceberg volumes and melt rates, and to estimate iceberg keel depths. Iceberg movements, important for determining residence times of icebergs in fjords, location of freshwater input, and identifying broad circulation patterns, have been tracked with GPS transmitters (Sutherland, et al., 2014; Larsen et al., 2015). Currently, there are no fjord-wide descriptions of iceberg distributions. Additionally, the influence of glacial depth and calving style on iceberg properties has not previously been investigated.

Here, we use multiple satellite datasets to quantify and compare iceberg characteristics over larger spatial scales, for larger populations of icebergs ($n > 100000$) and over a wider size resolution (as small as 30 m length) than has previously been achieved. We describe the size-frequency distributions of icebergs, and calculate the volume of icebergs in three fjords. Our results provide robust constraints on iceberg size distributions and keel depths for use in numerical ocean models, and serve as a baseline estimate of iceberg melt.

I collected and processed all data used to quantify icebergs distributions and sizes in fjords. E. Enderlin constructed and provided raw digital elevation models which allowed me to calibrate iceberg size relationships as described in Chapter II. Additionally, data concerning glacial movement, which enabled comparisons between methods and discussion of seasonal effects, was provided by L. Stearns.

CHAPTER II

METHODS

The algorithms used to construct digital elevation models (DEMs) as described in this chapter were run by E. Enderlin. I was responsible for establishing DEM base elevations, locating and delineating icebergs, establishing area to volume relationships, and all of the writing.

L. Stearns provided glacier speeds and terminus positions obtained from satellite tracking as described under the seasonal calving flux heading. I was responsible for converting those data to ice calving fluxes and all the writing.

Overview

Using optical satellite imagery and position records from GPS units mounted on large icebergs we examine and compare total iceberg coverage, iceberg volume, and iceberg size distributions within and between three Greenlandic fjord systems. We classify icebergs in Landsat 8 (L8) images and calculate their areas, and we use high-resolution DEMs to calibrate an iceberg area to volume relationship. Additionally, we assume idealized iceberg shapes and calculate upper and lower bounds on iceberg keel depths.

Physical Setting

We examine three different glacial fjord systems in two separate coastal regions of Greenland: Sermilik Fjord (SF) in the southeast; and Rink Isbræ Fjord (RI) (also known as Karrats Isfjord) and Kangerdlugssûp Sermerssua Fjord (KS) on the west coast, both within the greater Uummannaq fjord system (Figure 1).

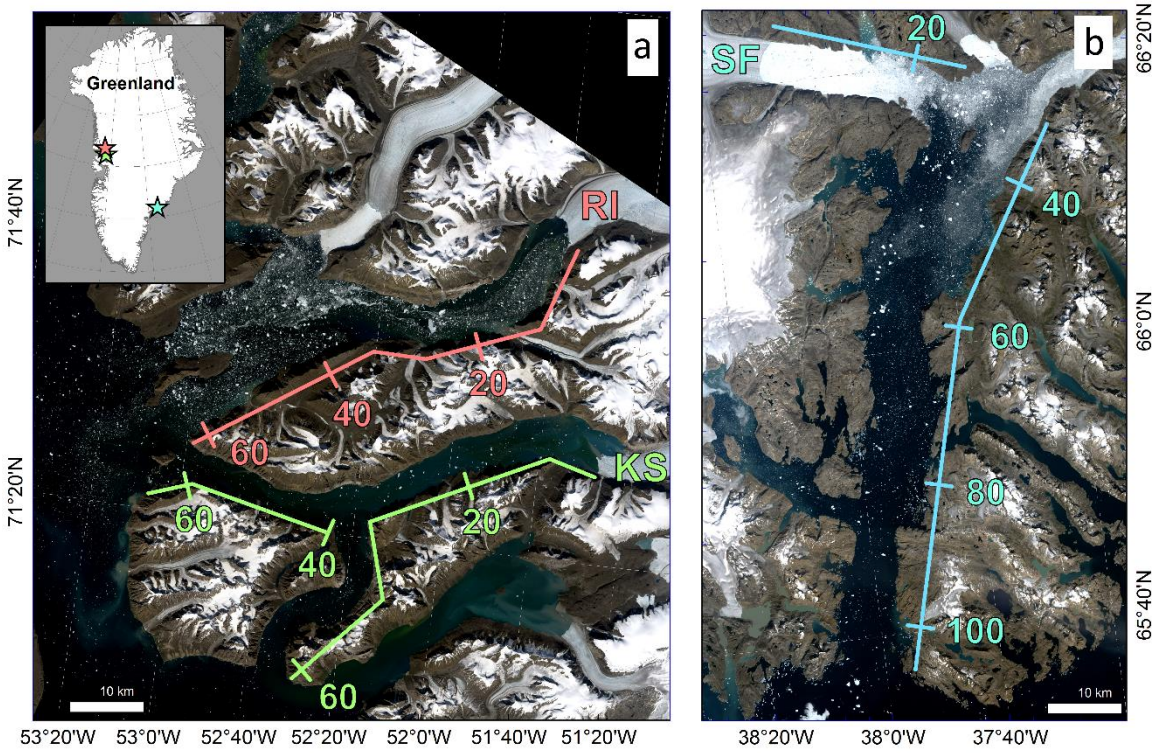

Figure 1: Layout of the three fjords. The location of the fjords in Greenland is shown (a, inset). RI and KS are shown in a L8 image from 7/8/14 (a), and SF is shown in a LS8 image from 8/7/14 (b). Distances (km) from glacial termini are shown along colored lines in both panels.

Sermilik Fjord (SF):

SF, located in southeast Greenland, is the outlet to the Irminger Sea for icebergs calved from Helheim Glacier (Figure 1). Helheim Glacier is a major outlet of the GrIS reaching speeds of 8-11 km yr^{-1} along its trunk, it is one of the GrIS's most prolific producers of icebergs (~25 Gt yr^{-1}) (Moon et al., 2012; Enderlin et al., 2014). The northern portion of the ~600 m deep, ~5.5 km wide terminus is periodically at or held below flotation, while the southern portion is grounded (Murray et al., 2015). Ice calved from Helheim Glacier travels approximately 20 km to the east through Helheim Fjord, often in a densely packed ice mélange, before entering SF. From the mouth of Helheim

Fjord, SF extends to the south for ~80 km to the Irminger Sea. SF ranges from 8-12 km wide and 600 – 900 m in depth, and has no shallow sill at its mouth. During summer, the fjord generally contains a layer of relatively cold (~0.5° C) and fresh Polar Water to depths of ~100 – 200 m, above a layer of warmer (up to 4° C) , saltier Atlantic Water (Sutherland et al., 2014). SF has been the subject of many investigations on its circulation and hydrography (Straneo et al., 2010; Sutherland et al., 2014), calving dynamics (Murray et al., 2015), and iceberg motion (Sutherland et al., 2014), melting (Enderlin & Hamilton, 2014), and keel depth (Andres et al., 2015). Hereafter, we will refer to the entire system between Helheim Glacier and the Irminger Sea as SF.

Rink Isbræ Fjord (RI):

RI, located in west Greenland, is the fjord into which Rink Isbræ (glacier) terminates (Figure 1). Rink Isbræ has an average speed of ~4.2 km yr^{-1} near its 4.7 km wide terminus. The glacier is partially floating, reaching a depth of 840 m in water deeper than 1000 m (Bartholomaus et al., 2016; Rignot et al., 2016). The fjord is 6 – 12 km wide and 1100 m deep along much of its depth, running primarily east to west for ~65 km between the terminus of Rink Isbræ and its mouth at the broader Uummannaq fjord system. Karrats Island splits the end of the fjord into north and south arms ~50 km down-fjord from the glacier terminus. On the southeast side of the island there is a sill with a depth of 430 m, while on the island's north side a sill rises to ~230 m below the surface. RI contains cold (~1° C) fresh water to depths of 100 – 200 m overlaying warmer AW with temperatures up to 3° C (Bartholomaus et al., 2016).

Kangerdlugssûp Sermerssua Fjord (KS):

KS is the next fjord containing a marine-terminating glacier to the south of RI (Figure 1). Despite its close proximity, KS has significantly different properties than RI. The glacier moves much slower (~1.8 km yr^{-1}) and is only 4.2 km wide and 250 m deep at its terminus, where it is grounded (Rignot et al., 2016). The fjord runs generally east to west for ~63 km before opening to the Uummannaq fjord system. At 37 km down-fjord from the glacier terminus the fjord splits into north and south arms. KS is much shallower than RI, reaching depths of only about 500 m. At the mouth of the north arm there is a sill at a depth of 430 m, and another sill rises to 290 m depth on the near-glacier end of the south arm. Waters in KS are generally colder than those at corresponding depths within RI, with waters near 0° C to 100 m depth overlying waters up to 2° C (Bartholomaus et al., 2016).

Landsat 8 Image Processing

We collected all cloud-free L8 images of SF, RI, and KS captured between 2013 and 2015 (Table 1). Images in which fjords contained substantial sea ice (i.e., images from before July 1st in SF and before July 15th in RI and KS each season) were not used. We used the panchromatic band (band 8) in each scene to take advantage of its higher spatial resolution (15 m) compared to other bands (30 m). We masked land and coastal areas outside of the fjords in each image, and all analyses were carried out only on ice and water within the fjords. Icebergs were delineated and measured using a combination of tools available in ArcMap and Orfeo Toolbox (OTB). Briefly, we defined pixels containing ice as those having a brightness above a certain threshold, and found the total area of ice coverage for each image. We then combined adjoining ice pixels into

polygons. Those polygons that contained multiple icebergs were split into individual icebergs either by hand or using a texture analysis technique where icebergs and iceberg edges stand out as irregular from background ice mélange. Details regarding each step of the iceberg identification and delineation are presented below.

Table 1: Total ice coverage and total area and volume of classified icebergs for each analyzed image.

Image Date	Image Coverage	Total Ice Area km^2 (Percent of Fjord Surface)	Total Iceberg Area Classified via Threshold km^2 (Percent of Total Ice)	Total Iceberg Area Classified via SFS km^2 (Percent of Total Ice)	Area of Small (L<15m) Ice Pixels Removed km^2 (Percent of Total Ice)	Total Volume of Classified Icebergs km^3
SF						
9/3/13	Mouth to 60 km up fjord	14 (2.3)	12.7 (91)	0 (0)	0.53 (4.4)	1.22
7/4/14	Mouth to 60 km up fjord	33 (7.7)	26.0 (71)	0.9 (2)	1.67 (5.1)	2.37
8/7/14	Full Fjord	170 (18)	26.9 (16)	9.6 (6)	1.50 (0.9)	3.93
9/15/14	Full Fjord	271 (29)	24.4 (9)	28 (10)	1.26 (0.5)	6.15
9/22/14	Full Fjord	294 (31)	42.8 (15)	19 (6)	1.58 (0.5)	7.08
7/7/15	Full Fjord	209 (22)	56.8 (27)	18 (8)	2.99 (1.4)	7.45
7/16/15	Full Fjord	305 (32)	43.4 (14)	29 (9)	2.38 (0.8)	7.52
RI						
8/20/13	Full Fjord	7.2 (1.3)	7.0 (97)	0 (0)	0.40 (5.6)	1.22
8/22/13	Glacier to 30 km down fjord	8.7 (4.2)	6.1 (70)	0 (0)	0.07 (0.9)	1.04
9/16/13	Glacier to 30 km down fjord	1.1 (0. 5)	1.0 (92)	0 (0)	0.01 (0.9)	0.15
8/7/14	Full Fjord	52.2 (9.4)	17.1 (33)	0 (0)	0.59 (1.1)	2.02
7/18/15	All except westernmost 10 km	14.1 (2.8)	11.2 (79)	0 (0)	0.30 (2.1)	1.45
8/26/15	Full Fjord	40.0 (7.2)	11.4 (29)	1.59 (4)	0.38 (1.0)	1.48
9/13/15	Full Fjord	128.3 (23.1)	11.0 (8)	8.6 (7)	0.56 (0.4)	2.04
KS						
8/20/13	Full Fjord	2.10 (0.53)	1.24 (59)	0 (0)	0.02 (1.0)	0.14
8/2/14	All except western 15 km of north arm	3.10 (0.87)	1.97 (64)	0 (0)	0.03 (1.0)	0.28
8/7/14	Full Fjord	2.39 (0.60)	1.75 (73)	0 (0)	0.03 (1.3)	0.16
9/17/14	Full Fjord	0.53 (0.13)	0.52 (98)	0 (0)	0.02 (3.8)	0.04
7/18/15	Full Fjord	5.03 (1.27)	3.01 (60)	0 (0)	0.06 (1.2)	0.30
7/20/15	All except western 15 km of north arm	2.54 (0.71)	2.52 (99)	0 (0)	0.03 (1.2)	0.29
7/27/15	Full Fjord	2.92 (0.74)	2.41 (83)	0 (0)	0.03 (1.0)	0.26
8/5/15	All except western 15 km of north arm	2.28 (0.64)	2.02 (89)	0 (0)	0.04 (1.8)	0.22
8/26/15	Full Fjord	1.45 (0.37)	1.35 (94)	0 (0)	0.03 (2.1)	0.13
9/13/15	Full Fjord	1.82 (0.46)	1.28 (70)	0 (0)	0.03 (1.6)	0.11

Total Ice Area

All ice was first delineated using a thresholding technique. L8 image data are distributed by the USGS as scaled digital numbers (DN), the values and ranges of which vary between images depending on the sun elevation angle (SE) at the time the image was taken. To obtain a standard threshold to use across all images, we converted seven images from DN to values of top of atmosphere (ToA) reflectance using the method described by the USGS (2016). By inspecting the ToA reflectance values of at least 40 pixels, half of which clearly contained ice, and the other half of which clearly contained water, distributed throughout each converted image, we determined that a threshold reflectance of 0.28 W m^{-2} robustly separated pixels containing ice from those containing water. For all images, we then found the DN value corresponding to a top of atmosphere (ToA) reflectance value of 0.28 W m^{-2} using the formula:

$$DN = \frac{\sin(SE) * .28 - RAV}{RMV}$$

where *RAV* is the reflectance add value, and *RMV* is the reflectance multiplication value (USGS, 2016). The values of *SE*, *RAV*, and *RMV* are distributed with the metadata of each L8 scene. Pixels with values higher than the threshold DN were defined as ice. Adjoining ice pixels were converted into polygons, and their areas were calculated (Figure 2, b and c). We summed the areas of all ice polygons to calculate the total fjord area covered in ice for each image. To compare ice coverage and iceberg properties within fjords, we split fjords into bins of roughly equal distance from the termini and found the area of ice coverage within each bin. Mean lengths of bins are 3 km in SF and RI and 5 km in KS.

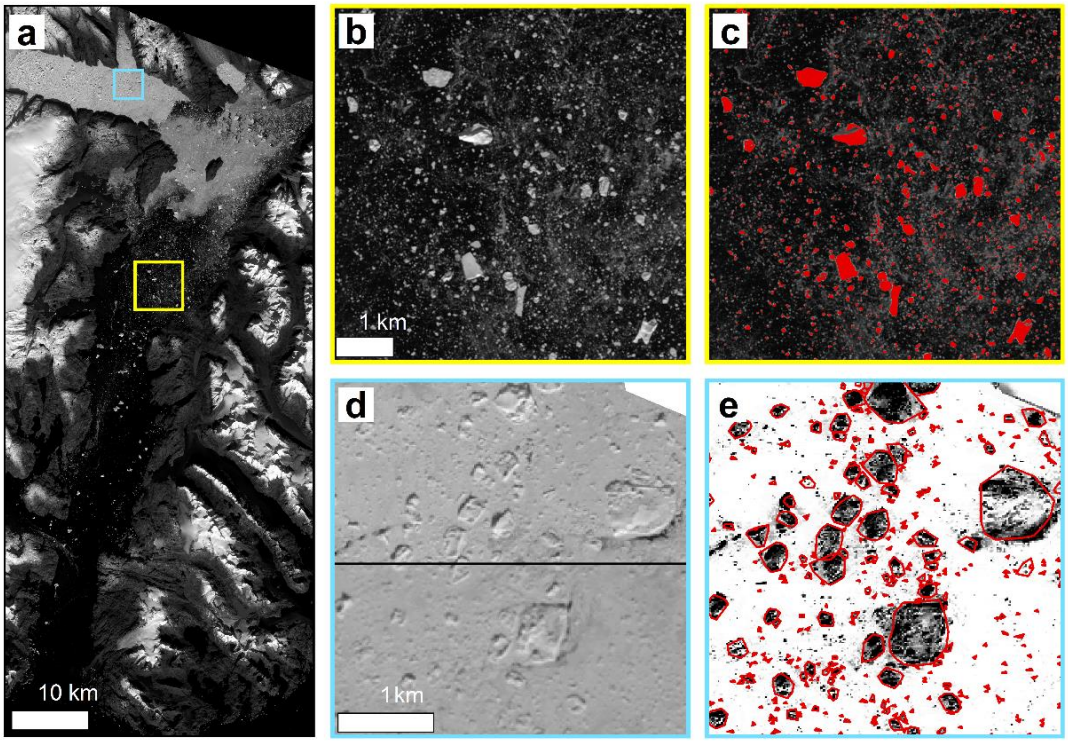

Figure 2: The iceberg classification process. **(a):** Band 8 of an L8 image from 9/15/14 containing SF is shown with the extents of panels (b) and (c) outlined in yellow, and (d) and (e) outlined in blue. **(b):** Individual icebergs are surrounded by open water throughout much of the fjord. **(c):** Pixels with a DN above an equivalent TOA reflectance of 0.28 W m^{-2} (DN > 11412 in this image), shown in red, are defined as ice and iceberg polygons are defined. **(d):** Areas with ice mélange (upper half) are smoothed using a boosted-mean filter (lower half). **(e):** The "length" output of an SFS extraction run on the filtered image is shown in black and white. Pixels with low SFS-Length values are defined as belonging to icebergs, and minimum bounding convex hull polygons (red outlines) are built around adjoining pixels to define iceberg extents.

Individual Iceberg Separation and Classification

We split ice polygons containing multiple icebergs into individual icebergs using two different methods. Iceberg boundaries are visible in L8 images as linear regions that are slightly lighter or darker than their surroundings (Figure 2d). In order to avoid multiple adjacent icebergs being counted as a single iceberg, we visually inspected all polygons created by the above thresholding method that had areas greater than 20000 m^2

and identified polygons containing multiple icebergs. Those polygons were then either split into individual iceberg polygons manually using editing tools in ArcMap, or the data was clipped and exported to a separate raster file. Single pixels that were above the threshold but not adjacent to any other pixels that were also above the threshold were removed. Many of those single pixels would only be partially filled with ice, and identifying them all as icebergs with a length of 15m would lead to large overestimations of total ice volume. Additionally, eliminating ice pieces with lengths < 15 m (1 pixel in L8 images) limits our analyses to ice defined as icebergs, as smaller pieces are known as growlers and bergy bits (NSIDC, 2016).

To delineate icebergs in ice mélange, we first applied a boosted mean filter to the raster datasets containing the ice mélange to minimize noise in images while retaining iceberg edges (Figure 2d) (Williams & Macdonald, 1995). The filter is made up of two steps: first, a 3x3 low-pass filter is applied to the pixels in which each pixel is assigned a new value equal to the average of itself and the 8 pixels with which it shares vertices; the result of the low pass filter is then averaged with the original image.

As the second step to delineate icebergs in ice mélange, we used the structural feature set (SFS) tool available in OTB on the result of the boosted mean filter (Figure 2e) (Huang et al. 2007). Because of differences in DN ranges, lighting, shadows, and ice mélange surface between images we were unable to use standardized values for spectral and spatial thresholds. Instead, we used an iterative process in which for each mélange image we ran the SFS tool several times using 20 directional lines and varying the spectral (2500 – 5000 DN) and spatial (12 – 50 pixel) thresholds. For each pixel in the dataset (the central pixel), the spectral difference between the central pixel and the

nearest pixel along each of 20 equally spaced direction lines is determined and the line is extended if that difference does not exceed the spectral threshold and the distance between the pixels does not exceed the spatial threshold. Otherwise the extension of the direction line is terminated. The lengths of the direction lines are defined as the distance in pixels between the endpoints of each line, and the first band of the output of the SFS tool (SFS-length) is the maximum length of the 20 direction lines. We visually inspected the first band of the resultant outputs and determined which threshold combination best separated individual icebergs from the ice mélange for each image. Icebergs, and especially iceberg edges, generally display less uniformity than the surrounding mélange, therefore pixels within, or at edges of, icebergs had low values of SFS-length (Figure 2e). Pixels that were assigned an SFS-length value below a certain threshold that was determined by visually inspecting each image individually were defined as iceberg pixels. We combined adjoining iceberg pixels into polygons and calculated their areas. We inspected all icebergs with an area greater than 20000 m^2, and manually split up polygons containing multiple icebergs. We then replaced iceberg polygons with the minimum bounding convex hull that contained all iceberg pixels in order to fill doughnut holes and connect unclosed outer boundaries (Figure 2e).

We examined the efficiency of using the SFS tool to delineate icebergs by comparing the results to a manual classification method. We visually inspected a 16 km^2 region of ice mélange in each of 5 L8 images and manually delineated all icebergs that could be seen that were completely within the region for each image. We compared total ice area and iceberg size distribution of the two methods. The manual iceberg delineation process cannot be considered to be 100% accurate, as small icebergs and the edges of

many icebergs often cannot easily be seen in L8 images even with visual inspection. Therefore, we also inspected and delineated by hand icebergs that could be seen within a 5.4 km^2 region of ice mélange from a very-high resolution (0.5 m) Worldview image from 7/6/16.

Non-iceberg Ice Correction

The thresholding technique used to define ice in L8 images does not differentiate between icebergs and sea ice or rafts small pieces of ice. Therefore, we quantified the proportion of total ice delineated by the thresholding technique that was made up of icebergs in very-high resolution imagery from Worldview satellites. In SF we analyzed either a 3 km^2 region where ice concentrations were high near the ice mélange (images from 8/21/11 and 6/29/12) or a 12 km^2 region where ice concentrations were lower in the open fjord (images from 7/15/10, 7/11/13, 7/30/13, 8/15/12, and 6/8/15). In RI we analyzed a 16 km^2 region in images from 6/25/13, 7/4/13, 7/17/13, 8/11/13, and 7/19/14, and in KS we analyzed an 18 km^2 region in images from 6/25/13, 7/4/13, and 7/17/13. We used a thresholding technique as described above to delineate ice polygons, then visually inspected each ice polygon to determine whether it was an iceberg or other form of ice (sea ice or conglomeration of brash ice, bergy bits, etc.).

Area – Volume Relationships

We constructed DEMs of icebergs in SF to establish a relationship between iceberg area and volume. Eight DEMs were generated using very high resolution (~0.5 m) stereo imagery from the Worldview 1 – 3 satellites. We created DEMs using either the NASA Ames Stereo Pipeline (ASP) (Moratto et al., 2010) or the Surface Extraction with TIN-based Search-space Minimization (SETSM) (Noh & Howat, 2015) algorithms

(Table 2). Comparisons between DEMs generated by the two algorithms revealed random, non-systematic differences, justifying the merger of the two DEM datasets. All DEMs have a horizontal resolution of ~2 m and random errors of 3 m (Enderlin & Hamilton, 2014).

For each DEM we manually created polygon boundaries around icebergs using ArcMap software. We then found the area and average elevation of each polygon. We calculate the elevation of the ocean surface by taking the average elevation of at least ten ice-free pixels dispersed throughout each DEM, and subtracted that elevation from the mean elevation of pixels making up each iceberg. We multiplied that mean elevation with the visible area of each iceberg to find its above water volume. Assuming an iceberg density of 920 kg m^{-3} and a fjord-water density of 1025 kg m^{-3}, we calculated the underwater volume and total volume of each iceberg (Figure 3). We then fit all DEM data using the general power law:

$$V = aA^b$$

where V is the calculated iceberg volume, A is the measured iceberg area, and a and b are empirically derived constants of best fit.

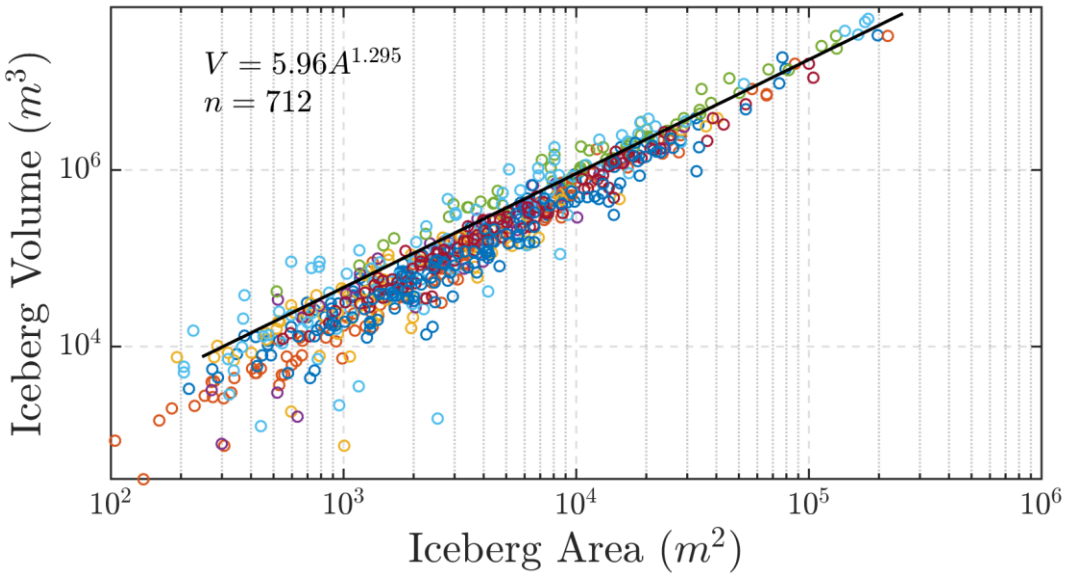

Figure 3: Iceberg areas vs volumes data and fit of data from DEMs. Points are individual icebergs, and different colors represent different DEMs. The black line is the best fit of all data, and its equation is displayed.

Iceberg Characteristics and Size Distributions

We used a ranked size distribution of iceberg volumes to quantify the distribution of iceberg volumes within fjords. For each fjord, we assigned each iceberg a sequential rank, starting with the lowest volume iceberg as "1", the second lowest as "2", and so on until all icebergs were ranked. When icebergs had identical volumes, they were assigned a rank equal to the mean of what their ranks would have been had they all been unique (e.g. if icebergs 3, 4, and 5 all had equal values they would all be assigned the rank of 4). We observed many small icebergs with identical volumes, so our first rank number was in the hundreds to thousands. We then tested the fit of several types of distributions relating individual iceberg volume to the proportion of icebergs with a greater volume in order to compare observed distributions to previous work and to determine the best fit to observations.

To approximate iceberg depths we used two different shapes to set lower and upper bounds for classified icebergs. For a minimum depth bound, we use a simple block type shape in which icebergs maintain the same cross sectional area (A) displayed at the waterline throughout their depths (d). To calculate a maximum bound we use the lesser of the height of an inverted elliptical cone with a major axis length (L) equal to the measured major axis for each iceberg and a minor axis (B) equal to $\frac{4A}{\pi L}$, and $1.43L$, which has been observed as an upper boundary for keel depths relative to lengths (Hotzel & Miller, 1983; Dowdeswell & Forsberg, 1992). Real, non-tabular icebergs have variable shapes rather than maintaining a consistent shape throughout their depths or extending to a pointed cone (Robe, 1980; Barker et al., 2004). Therefore, all real iceberg keel depths fall somewhere between these two end members. For an iceberg with volume V, area A, and length L, its depth d is:

$$\frac{V}{A} < d < \begin{cases} \frac{3V}{A} \\ 1.43L \end{cases}$$

As a measure of how variable iceberg sizes are throughout each fjord and between different regions within each fjord we compare the standard deviation of iceberg areas within different regions of the fjords for each image. We also compare those values across different images to identify patterns that are consistent over time for each fjord.

Seasonal Calving Flux

The calving flux represents the amount of ice lost at the terminus through both iceberg calving and submarine melting over time. To calculate calving fluxes we multiplied the calving rates by the width and depth of the glacial termini. To determine calving rates, we average velocity values across the width of each glacier terminus. For

each velocity epoch, we calculate the calving rate (c) using the width-averaged terminus velocity (U_M), and the width-averaged change in terminus position (L) between each velocity epoch:

$$c = U_M - \frac{dL}{dt}$$

Velocity data are derived from a combination of radar (Joughin et al., 2010; Joughin et al., 2011) and optical imagery (Rosenau et al., 2015); terminus position data were semi-automatically derived using both radar and optical imagery (after Foga et al., 2014). To determine the seasonal calving rate, we resampled the data to monthly averages before calculating the calving rate.

Iceberg Trackers

Following methods established by Sutherland et al. (2014) we deployed either Axonn AXTracker GPS or GeoForce GT1 GPS tracking units from helicopters onto large (>100 m) icebergs. In SF, 5 trackers were deployed in 2012, 2013, (data presented by Sutherland et al., 2014), and 2014, and 10 trackers were deployed in 2015. In RI, 3 trackers were deployed in 2013. In KS, 3 trackers were deployed in 2013, and 4 were deployed in 2014.

CHAPTER III

RESULTS

Area-Volume Relationships

We first present the results of creating DEMs and establishing a relationship between iceberg area and volume to provide necessary context for other results. Iceberg volume was strongly correlated with cross-sectional area in all eight DEMs generated using images in SF (Figure 3). Combining data from all DEMs, we found the relationship between cross-sectional iceberg area (A) at the waterline and iceberg volume (V) to be:

$$V = 5.957A^{1.295}$$

We use this relationship to convert all iceberg areas to volumes for use in further analyses. Results of fitting power laws of the same form ($V = aA^b$) to individual DEMs resulted in values ranging from 0.94 – 30.09 for the scalar a, and from 1.15 – 1.44 for the exponent b (Table 2).

Table 2: Coefficients and R2 values for power law fits relating iceberg area to volume for each DEM created.

Date	DEM Creation Algorithm	Number of icebergs measured	a (±95% confidence bounds)	b (±95% confidence bounds)	R^2
3/19/11	SETSM	108	30.09 (20.81)	1.15 (0.06)	0.96
8/21/11	ASP	118	17.07 (8.28)	1.18 (0.04)	0.98
8/24/11	ASP	75	0.94 (0.93)	1.44 (0.10)	0.98
6/10/12	ASP	39	1.80 (4.65)	1.39 (0.13)	0.95
6/24/12	SETSM	56	11.21 (22.47)	1.25 (0.09)	0.97
6/29/12	ASP	101	2.95 (2.93)	1.37 (0.08)	0.99
7/31/14 – (1)	SETSM	103	2.78 (2.38)	1.33 (0.08)	0.95
7/31/14 – (2)	SETSM	112	2.60 (2.27)	1.44 (0.08)	0.95
All Together		712	5.96 (2.59)	1.30 (0.04)	0.92

Fjord Ice Cover

In SF, the total percentage of fjord covered in ice ranged from 2.30 – 33.96% (Figure 4). Ice covered up to 100% in the mélange that stretches 20 km down-fjord from the terminus of Helheim Glacier (Figure 4). Other regions of consistently high ice

coverage exist around the island at the north end of the fjord and, to a lesser extent, at the mouth (Figure 5). Beyond the proglacial mélange, ice coverage decreases until reaching a distance of 50 km from the Helheim terminus. Coverage of ice then remains steady throughout the remainder of the fjord with the exception of the area near the mouth of the fjord, where ice from the shelf may be transported into the fjord.

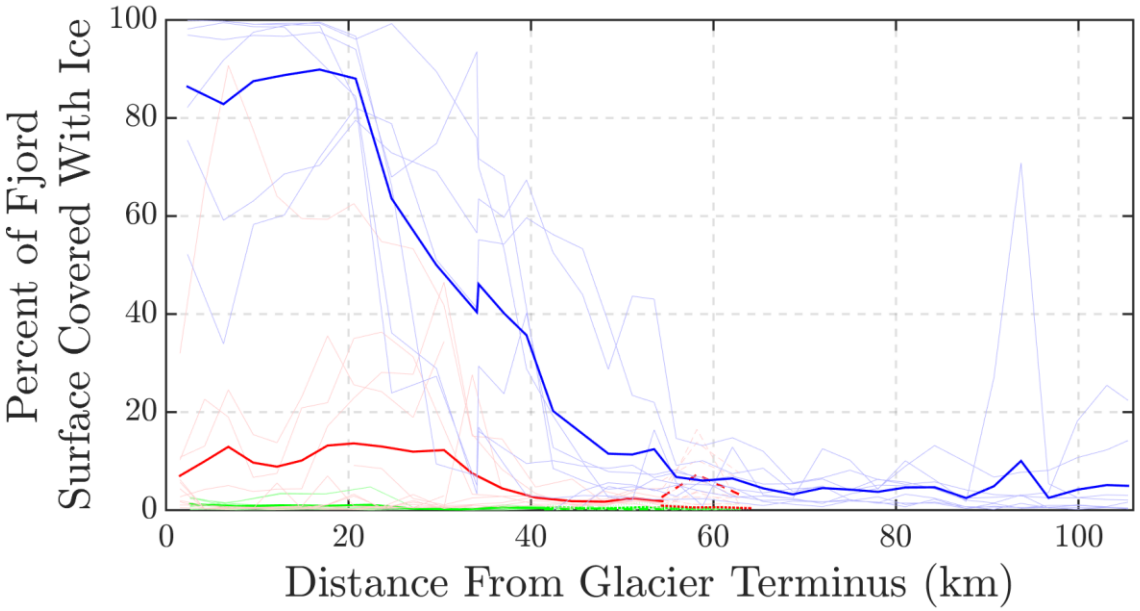

Figure 4: Percentage of fjord surface covered in ice for all images analyzed. Faint lines represent individual images, and bold lines are averages of all images for each fjord. Data from SF are blue, RI are red, and KS are green. In RI and KS, dashed lines represent the northern arms of the fjords, while dotted lines represent the southern arms.

In RI total ice coverage ranged from 1.11 – 23.12% of the fjord surface. Two regions had ice concentrations higher than in the remainder of the fjord: near the glacier terminus and in the north arm of the split (Figure 4). Ice concentrations in RI are notably higher to the north than the south, suggesting that the majority of ice flows outward through the northern half of the fjord and/or that ice becomes grounded on the shallower sill there and thus spends more time in that region (Figure 5).

KS had less than 2% of its surface covered with ice in all images (Table 1). Ice coverage was highest near the glacier terminus, and coverage was slightly higher in the south arm of the fjord than the north (Figure 4, Figure 5).

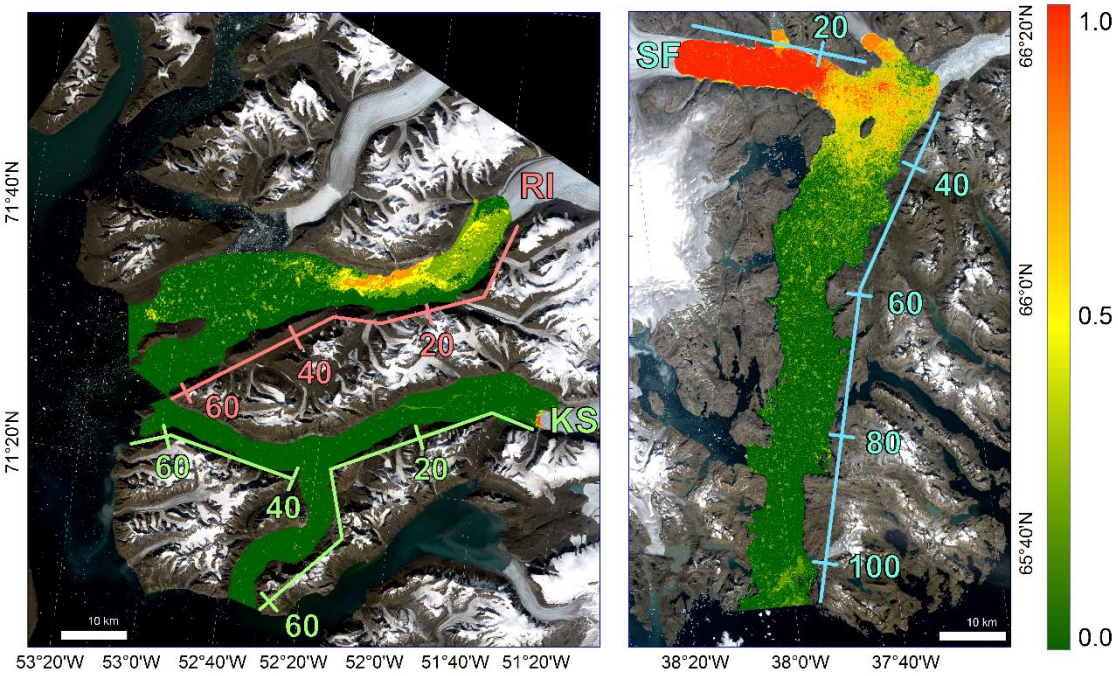

Figure 5: Probability of ice presence in full fjord images from later than July 15th in RI (4 images) and KS (7 images) (left panel) and later than July 1st in SF (5 images) (right panel).

The total amount of ice that we classified and measured as icebergs ranged from 16-99% of the total area of ice coverage (Table 1). Ice that was not classified was either ice in ice mélange that did not have boundaries that were detected by our method, single pixels that were above the brightness threshold for ice but were not adjacent to any other ice pixels, or classified icebergs that were subsequently removed as described below to account for sea ice captured by our thresholding method.

In SF, sea ice made up 42% of the total calculated volume of ice in the image that we analyzed from June 8, 2015. In all other images sea ice made up an average of 3.31% (ranging from 0.39 – 9.12%) of the total calculated volume of ice. We therefore removed L8 images acquired before July of each year. In images from July 1st or later, we used the "randsample" command in Matlab to remove a random sample of the total set of delineated icebergs from each of four size classes. We removed 7.88% of icebergs that are between 0 and 100000 m^3, 7.79% of icebergs between 100000 and 200000 m3, 3.64% of icebergs between 200000 and 300000 m^3, and 4.14% of icebergs with volumes greater than 300000 m^3.

In RI, sea ice made up 33.4% and 11.8% of the total calculated volume of ice in the images that we analyzed from 6/25/13 and 7/4/13, respectively. Sea ice made up an average of 2.29% (ranging from 0 – 2.73%) of the total calculated volume of ice in Rink in images from later in the season than July 15. We therefore removed L8 images acquired before July 15th of each year, and removed a portion of icebergs delineated via the thresholding technique in L8 images from July 15th or later each year. Because total ice amounts were lower in RI than in SF we identified sea ice amounts in two rather than four size classes. We used Matlab to remove 7.44% of icebergs that are between 0 and 300000 m^3 and 4.55% of icebergs with volumes greater than 300000 m^3. We removed the same proportion of icebergs in L8 images from KS as total ice amounts in KS were too low to independently derive robust correction factors from high resolution images there.

We calculated volumes of individual icebergs and the total volume of classified icebergs present in each image. Total volumes of classified icebergs range from 2.40 – 7.52 km^3 (1.22 – 6.77 m^3 km^{-2} and 8.34 – 14.08 m^3 km^{-2} in open fjord and ice mélange,

respectively) in SF, 1.04 – 2.04 km^3 (0.73 – 5.02 $m^3\ km^{-2}$ and 4.11 – 6.61 $m^3\ km^{-2}$ in open fjord and ice mélange, respectively) in RI, and 0.04 – 0.30 km^3 (0.10 – 0.81 $m^3\ km^{-2}$) in KS (Table 1**,** Table 2). In all three fjords, we calculated greater total volumes of ice in images from earlier in the year (Figure 6). We fit linear regressions to data of ice volumes versus date, and found the total volume of ice decreases at rates of 0.57 $m^3\ km^{-2}\ month^{-1}$ in SF between July and late September, and 0.72 $m^3\ km^{-2}\ month^{-1}$ in RI, and 0.29 $m^3\ km^{-2}\ month^{-1}$ in KS from mid-July to mid-September.

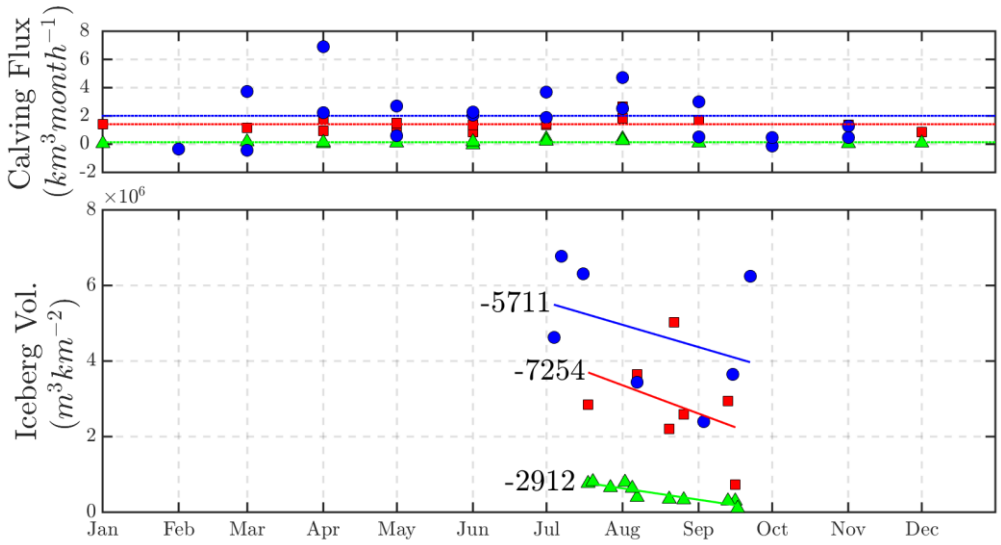

Figure 6: Calving flux (top panel) and total volume of classified icebergs observed in each image where the full fjord was visible (lower panel) throughout the year for SF (blue circles), RI (red squares), and KS (green triangles). Average annual calving fluxes are shown as dotted lines in the upper panel. Linear regression lines of best fit are shown on the lower panel and are annotated with their slopes ($km^3\ month^{-1}$).

Comparisons to manual classification of ice mélange reveal that the SFS method that we use tends to split large icebergs into several smaller icebergs (Table 3). We were unable to use the manual delineation method to define a robust correction factor as the resolution of L8 images is too low to accurately delineate all icebergs, and especially

small icebergs, present in the ice mélange of images. Iceberg volumes reported for areas of ice mélange are therefore lower bounds on the total ice present in ice mélange areas.

Table 3: Results of classifying 16 km^2 of ice mélange automatically and manually in each of five L8 images and 5.4 km^2 manually in one WV image.

			Number of Icebergs in Size Classes (10^5 m^3) per Area of Ice Mélange (km^2)				
	n (km^{-2})	**Iceberg Vol (10^5 m^3 km^{-2})**	**0 – 1 n (%)**	**1 – 2 n (%)**	**2 – 3 n (%)**	**3 – 4 n (%)**	**4 + n (%)**
Automatic Classification, All	29	131	24 (81.0)	2.4 (8.25)	0.89 (3.05)	0.49 (1.68)	1.8 (6.06)
L8 Manual, All	10	173	2.5 (24.9)	1.6 (15.6)	1.3 (12.9)	0.69 (6.88)	4.0 (39.8)
WV Manual, Single Image	30	473	16 (54.0)	2.6 (8.70)	2.0 (6.83)	0.37 (1.24)	8.7 (29.2)
Individual images							
8/7/14							
Auto	18	119	14 (80.8)	1.5 (8.54)	0.63 (3.56)	0.31 (1.78)	0.94 (5.34)
Manual	9.6	161	3.0 (31.2)	1.7 (17.5)	1.1 (11.7)	0.75 (7.79)	3.1 (31.8)
7/7/15							
Auto	31	60.3	24 (78.9)	2.4 (7.99)	0.88 (2.87)	0.69 (2.25)	2.4 (7.99)
Manual	10	82.0	2.9 (29.2)	1.6 (15.5)	1.2 (11.8)	0.50 (4.97)	3.9 (38.5)
7/16/15							
Auto	20	116	15 (76.7)	2.1 (10.5)	0.75 (3.83)	0.31 (1.60)	1.4 (7.35)
Manual	8.5	175	2.3 (26.5)	0.69 (8.09)	1.2 (14.0)	0.38 (4.41)	4.0 (47.1)
9/15/14							
Auto	41	145	34 (82.9)	3.5 (8.56)	1.2 (2.91)	0.75 (1.83)	1.6 (3.82)
Manual	13	192	2.9 (23.2)	2.8 (21.7)	1.6 (12.8)	1.0 (7.88)	4.4 (34.5)
9/22/14							
Auto	37	198	31 (82.9)	2.5 (6.77)	1.0 (2.71)	0.38 (1.02)	2.4 (6.60)
Manual	9.1	253	1.3 (14.4)	1.1 (12.3)	1.3 (14.4)	0.81 (8.90)	4.6 (50.0)

Iceberg Characteristics

SF had the widest range of iceberg properties seen in the three fjords, with lengths of individual icebergs ranging from 30 to 2547 m, as well as the lowest average iceberg size at a length of 66 m. KS had the smallest range of iceberg sizes (lengths 30 – 780 m) and the smallest maximum iceberg size of the three fjords, but the highest average iceberg length at 77 m. RI was intermediate in iceberg size range (length 30 – 1959 m), maximum size, and average length (70 m) (Table 4).

Table 4: Iceberg size and depth ranges for all images analyzed of SF, RI, and KS.

Fjord	SF	RI	KS
Length Range (Mean) [km]	30 – 2547 (67)	30 – 1959 (70)	30 – 780 (77)
Area Range (Mean) [100 m^2]	3 – 40300 (23)	3 – 10300 (30)	3 – 1870 (35)
Volume (Mean) [10^4 m^3]	0.98 – 11724 (22.8)	0.98 – 32585 (48.5)	0.98 – 4002 (50.2)
Maximum Vol. (Mean) [10^4 m^3]	4960 – 28890 (15590)	6650 – 36450 (23740)	598 – 4000 (15520)
Block Depth Range (Mean) [m]	28 – 257 (42)	28 – 300 (43)	28 – 186 (48)
Cone Depth Range (Mean) [m]	45 – 600 (91)	41 – 840 (96)	45 – 250 (107)
L:D Ratio Range (Mean) Blocks	1.06 – 47.4 (1.48)	0.97 – 6.78 (1.51)	0.70 – 5.69 (1.58)
L:D Ratio Range (Mean) Cones	0.70 – 15.8 (0.71)	0.70 – 2.31 (0.71)	0.70 – 3.12 (0.74)

Minimum areas of classified icebergs were bounded by the area of a simplified polygon incorporating two L8 pixels (304 m^2). Individual iceberg areas ranged to 860000 m^2 in SF, to 1030000 m^2 in RI, and to 187000 m^2 in KS. The average area of icebergs in SF, RI, and KS was 2310, 3030, and 3590 m^2, respectively (Table 4).

Iceberg keels depth estimates ranged from 28 – 257 m, 28 – 300 m, and 28 – 186 m in SF, RI, and KS, respectively, for block type icebergs (Table 4). For inverted cones, maximum depth estimates were truncated at glacial terminus depths (600 m in SF, 840 m in RI, and 250 m in KS), for 0.037, 0.009, and 8.61% of icebergs in SF, RI, and KS, respectively. All three fjord had significant proportions (1 – 27% in SF, 2 – 28% in RI, and 5 – 37% in KS) of icebergs reaching depths greater than 100 m, below which fjord waters begin to warm (Table 5, Figure 7).

Table 5: Combined number of icebergs (average number per image) reaching depths greater than 100 m observed in all images for each fjord.

Depth (m)	SF	RI	KS
100	1864 – 36058 (266 – 5151)	433 – 6514 (62 – 931)	208 – 1543 (21 – 154)
200	49 – 7898 (7 – 1128)	18 – 1528 (3 – 218)	0 – 549 (0 – 55)
300	1 – 1854 (0 – 265)	1 – 432 (0 – 62)	0 (0)
400	0 – 495 (0 – 71)	0 – 155 (0 – 22)	0 (0)

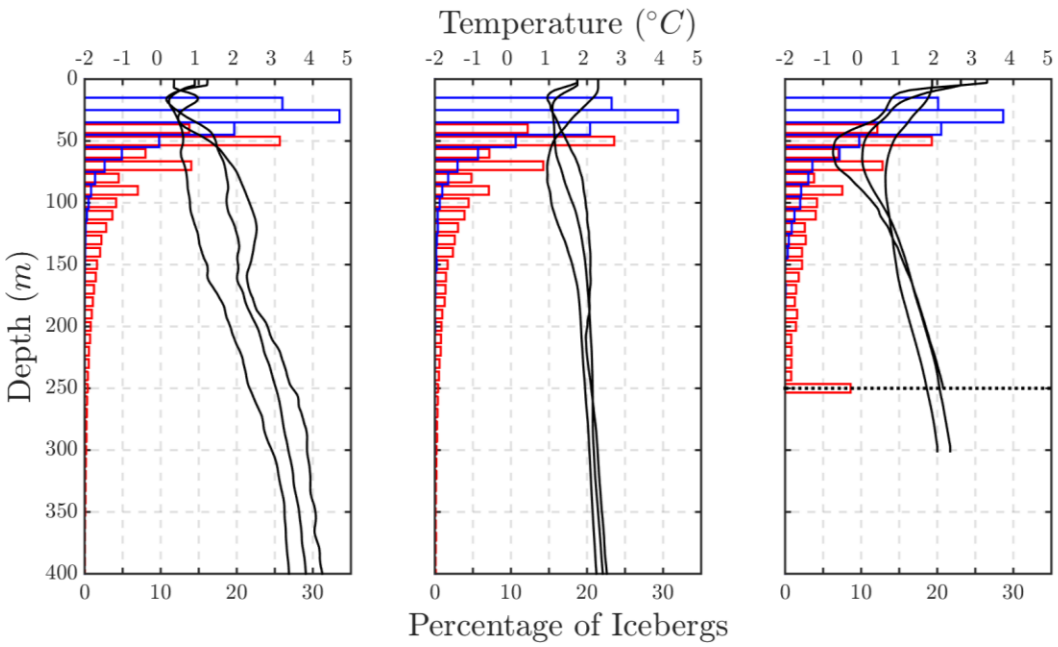

Figure 7: Percentage of icebergs reaching various depths (bars) and typical average temperature profiles during 3 separate summer seasons (black lines) for SF (left), RI (center), and KS (right) fjords. Blue bars represent minimum depths (block shape icebergs) and red bars are maximum depths (cone shaped icebergs). The depth of the grounding line at KS is shown as a dotted line in the right panel.

Iceberg Size Distributions

By number, all three fjords are dominated by small icebergs, but larger icebergs account for more of the total volume. The smallest icebergs (< 100000 m^3 (~65 m long)) typically make up more than two thirds of the total number of icebergs in all three fjords, but account for less than 10% of the total ice volume. By contrast, icebergs larger than 10^7 m^3 (~400 m long) account for just 0.28%, 1.41%, and 0.49% of the number of icebergs but 29.7%, 57.7%, and 14.1% of the total volume in SF, RI, and KS, respectively (Figure 8).

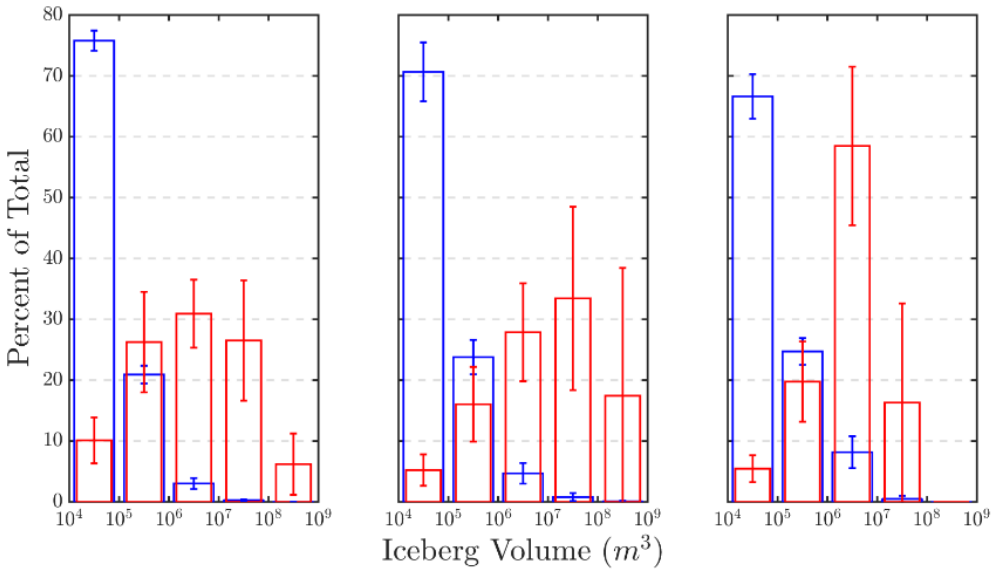

Figure 8: Average (bars) ± one standard deviation (error bars) of the total count (blue) and total volume (red) of classified icebergs across all images of SF (left), RI (center), and KS (Right).

Distributions of iceberg sizes have been described using power laws (Tournadre et al., 2016), Weibull distributions (Savage et al., 2000), and most often lognormal distribution laws (Wadhams, 1988; Dowdeswell & Forsberg, 1992; Tournadre et al., 2012, 2016), which have also been used to seed models (Bigg et al., 1997; Mugford & Dowdeswell, 2010). We examined the ability of the above distribution laws as well as the generalized Pareto distribution to describe our observations of iceberg volumes. The generalized Pareto distributions provided the best fit to the data (Figure 9). The survival function of the generalized Pareto distribution quantifies the probability (P) that the volume (V) of a randomly selected iceberg will be greater than a volume (v) and is given by the equation:

$$P(V > v) = \left(1 + \frac{\varepsilon v}{\sigma}\right)^{\frac{-1}{\varepsilon}}$$

where σ is the scale parameter and ε is the shape parameter. Fitting all icebergs from each fjord to generalized Pareto distributions resulted in values of 39926, 43738, and 51212 for σ and 0.8670, 1.0194, and 1.2857 for ε in SF, RI and KS, respectively (Figure 10,

Table **6**).

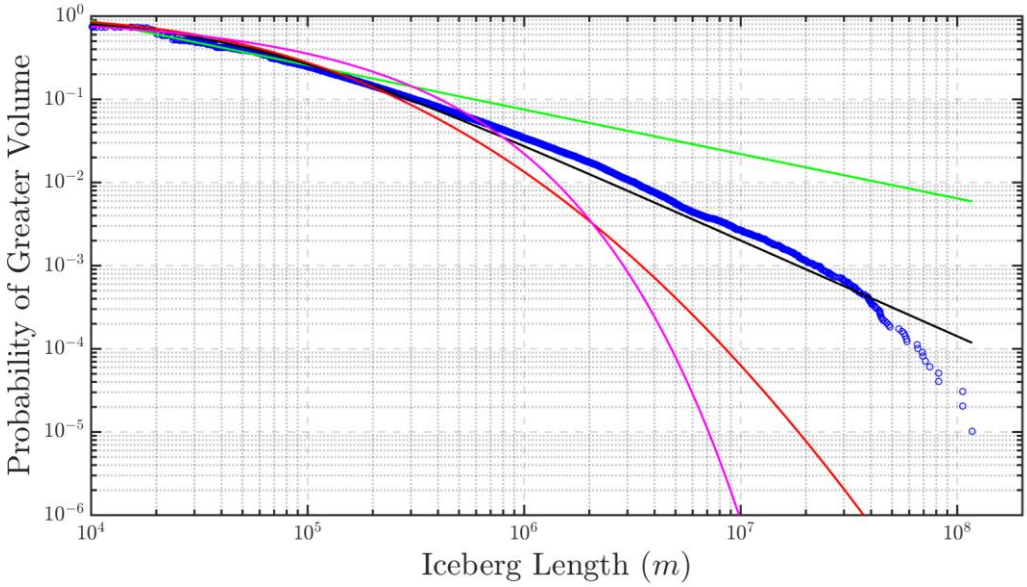

Figure 9: Iceberg volumes versus the probability of a randomly selected iceberg having a greater volume for icebergs delineated using thresholding in SF (blue circles) and lines of best fits to data for a power law (green), Pareto distribution (black), lognormal distribution (red), and Weibull distribution (magenta).

Table 6: Coefficients and goodness of fits for generalized Pareto distributions describing the probability (P) of a random iceberg having a volume (V) greater than v. Where P(V>v)=1+(εv/σ)^((-1)/ε)

Fjord	Iceberg Delineation Method (Threshold or SFS)	σ (±95% confidence bounds)	ε (±95% confidence bounds)
SF	Threshold	39926 (436)	0.8670 (0.0105)
	SFS	36923 (657)	0.9182 (0.0175)
RI	Threshold	43738 (1210)	1.0194 (0.0282)
	SFS	38151 (1568)	0.7637 (0.0410)
KS	Threshold	51212 (3017)	1.2857 (0.0655)

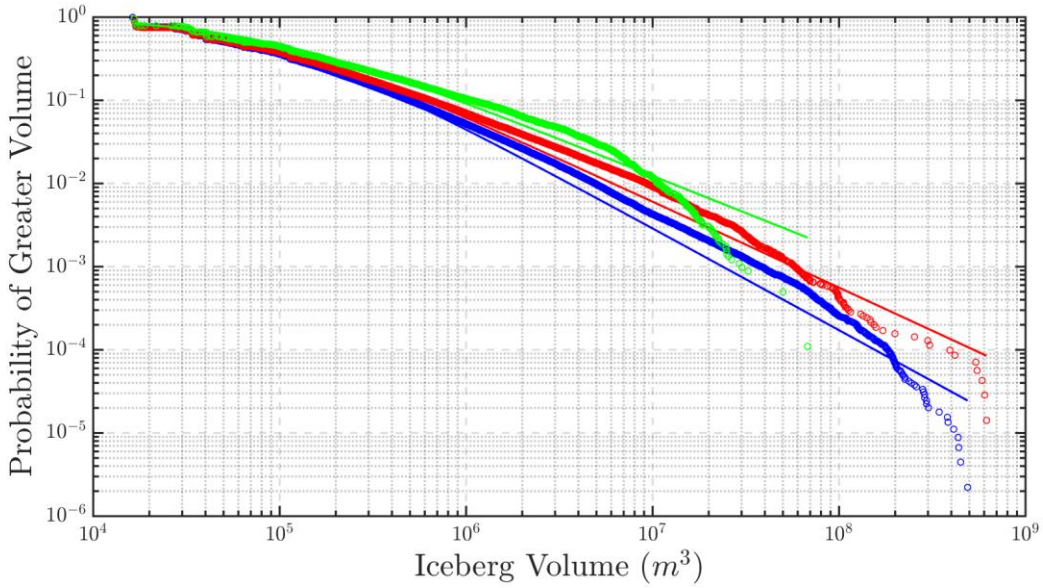

Figure 10: Volume distributions. Probability of a random iceberg being greater than a specified volume for SF (blue), RI (red), and KS (green).

We attempted the same distribution fits as above using iceberg lengths rather than volumes (Figure 11). Again, a Pareto distribution was best able to describe the data, but overall the model was not able to predict iceberg lengths as well as volumes. In particular, the abundance of large icebergs was under predicted by the model using length.

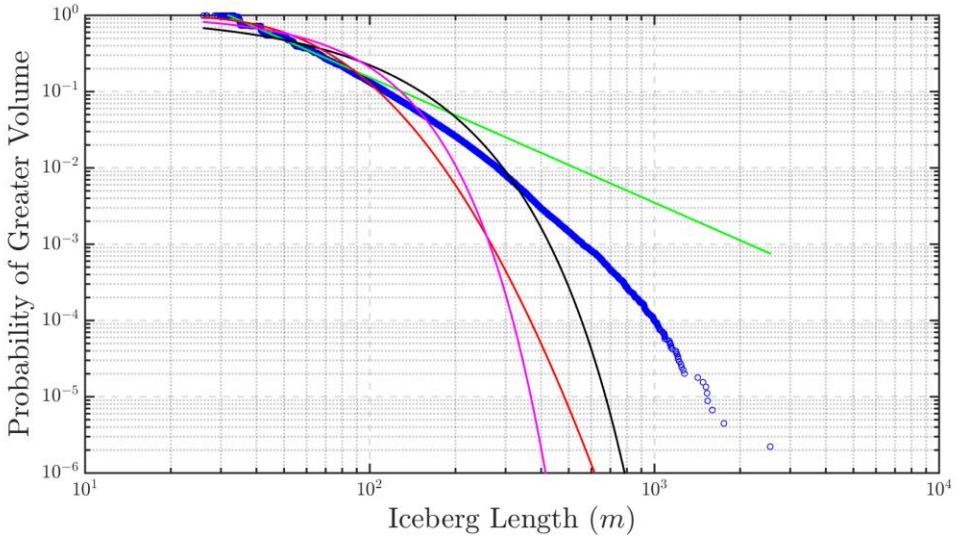

Figure 11: Iceberg lengths versus the probability of a randomly selected iceberg having a greater length for all icebergs observed in SF (blue circles) and lines of best fits to data for a power law (green), Pareto distribution (black), lognormal distribution (red), and Weibull distribution (magenta).

Ice Calving Flux

Ice calving flux is highest in SF (24 km^3 yr^{-1}), intermediate in RI (17 km^3 yr^{-1}), and lowest in KS (1.6 km^3 yr^{-1}) (Figure 6). In all three fjords, a seasonal signal was apparent with low or negative (meaning the glacier terminus is advancing without calving) fluxes throughout the winter, and higher than average calving fluxes occurring in the summer months, most notably in August. In the spring of both years in SF we observed one month with a high calving flux during the transition between lower winter calving rates and higher summer rates (45 km^3 yr^{-1} in March 2013 and 83 km^3 yr^{-1} in April 2014) (Figure 6).

Iceberg Trackers

Of all 25 trackers placed in SF, 13 transmitted positions throughout the fjord and eventually exited, five provided records within the fjord but stopped transmitting before exiting, and seven transmitted very limited or sporadic data that we do not use. Over the

entire fjord, the average residence time of icebergs was 132 days. Average residence time in the proglacial mélange for the 12 icebergs that we tracked there was 70 days, though it should be noted that we did not track these icebergs starting at Helheim Glacier, but rather 3 - 15 km down-fjord from the calving face. For the 13 icebergs that traversed the entire north-south portion of the fjord (beginning 20 km down-fjord from the terminus of Helheim Glacier) the average residence time in that region was 62 days. We observed icebergs recirculating primarily in two regions in SF: in the broad region between 35 and 55 km down-fjord of Helheim Glacier's terminus, where icebergs spent an average of 34 days, and in the region between the two constrictions from 64 to 86 km down-fjord from the Helheim Glacier, where icebergs spent an average of 23 days (Figure 12). Outside of the ice mélange, down-fjord motion was generally seen on the right (western) side of the fjord, while toward glacier motion was seen on the left (eastern) side.

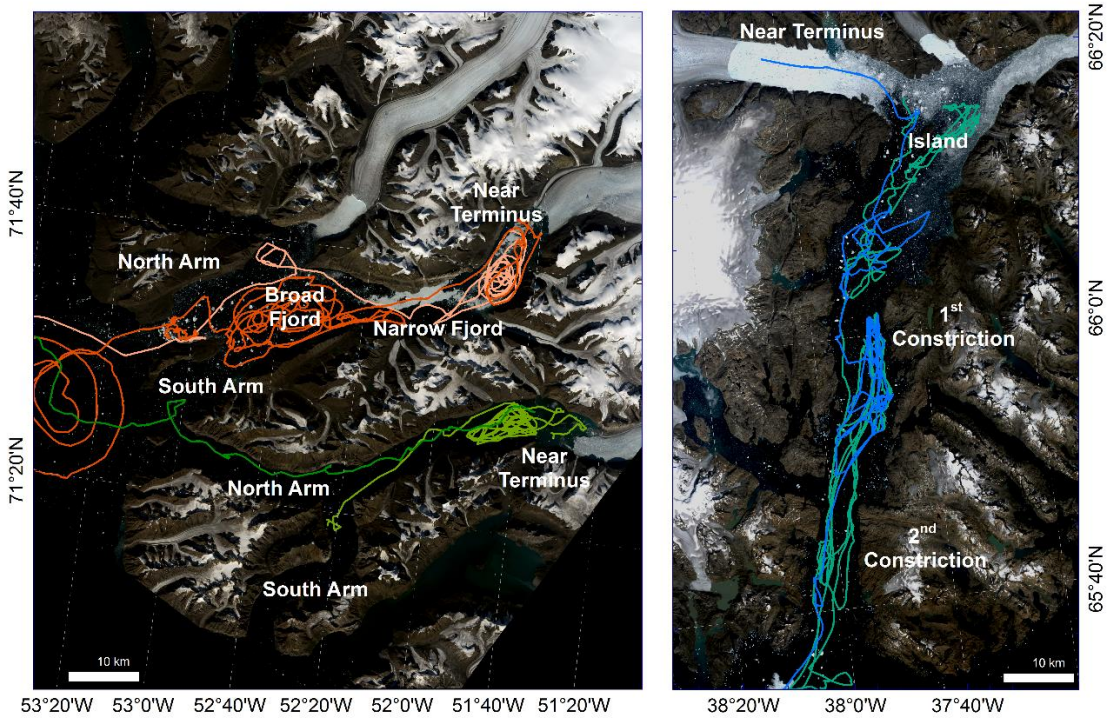

Figure 12: Example GPS tracker paths from RI and KS overlain on a L8 image from 7/8/14 (left), and from SF overlain on a L8 image from 8/7/14 (right).

In RI, two of the trackers that were placed on icebergs traversed the entire fjord and exited via the northern arm, while the third was lost after just two days. Residence times of the two tracked icebergs were 24 and 103 days. Both icebergs recirculated in the region between the glacier terminus and 16 km down-fjord of the terminus, spending 13 and 8 days there. One of the icebergs, UO07, subsequently exited 11 days after leaving that area, while the other, UO14, recirculated for 44 days in the broad region between 35 and 64 km down-fjord from the terminus before spending 51 days in the north arm of the fjord where it was likely grounded on the shallow (~240 m) sill, and eventually exiting (Figure 12). We observed UO14 in a Worldview 2 image from 9/16/13, and measured its

area to be 30913 m^2 and its length to be 300 m. Using these measurements we calculated the keel depth of the iceberg to be 126 – 377 m, confirming its potential to ground on the northern sill. For both icebergs, motion away from the fjord generally occurred on the right hand (northern) side of the fjord, while toward glacier motion occurred on the left hand (southern) side.

In KS, two icebergs that were tracked in 2013 traversed through the entire fjord and exited the north arm after 11 and 21 days. A third tracker only transmitted limited data for two days. In 2014 four trackers were deployed, one of which only transmitted data for two days so its data are not included. The three icebergs that were tracked all recirculated in the region between KS glacier and 20 km down-fjord, spending 17, 64, and >35 (the tracker that was in the zone for 35 days stopped transmitting before leaving the area) days there. Two of the icebergs then traveled down-fjord and one entered the southern arm of the fjord after five days, then stopped transmitting, while the other recirculated in the region between 20 and 30 km down-fjord for 20 days before entering the south arm and stopping transmissions 8 days later (Figure 12). Similar to SF and RI, down-fjord motion was generally observed on the right (northern) side of the fjord, and toward glacier motion was observed on the left (southern) side.

CHAPTER IV

DISCUSSION

Fjord Ice Volumes

Quantifying the volume of ice that resides within, and transports through, a fjord is essential to quantifying the GrIS freshwater flux and its influence on fjord and shelf water properties. *In situ* measurements of iceberg depths are difficult to obtain because icebergs can damage or destroy moorings and present hazards that preclude oceanographic vessels from a near approach. Even when those hazards are mitigated, any *in situ* measurements of depth are necessarily limited to small spatial scales (e.g. Andres et al., 2015) relative to what we can observe on the surface with satellite or aerial imagery. Establishing a relationship between iceberg areas visible in satellite or areal images and iceberg volumes is a solution that allows us to quantify volumes and depths of large numbers of icebergs.

We used an area to volume conversion as area is the property of icebergs that we directly measure that provides the greatest amount of information about iceberg size. To compare results to other studies, however, we also fit an empirical relationship between iceberg length (L) in meters and mass (M) in tonnes for 712 icebergs using the power law:

$$M = aL^b$$

In our relationship, $a=2.35$, $b=2.55$, and the correlation coefficient $R^2 = 0.93$. These results are similar to those of Hotzel & Miller, (1983) ($a = 2.009$, $b = 2.68$, $R^2 = 0.90$) who used 168 icebergs observed off Labrador, and Barker et al. (2004) ($a = 0.43$, $b =$

2.9, R^2 = 0.92) who used 14 measurements of 9 icebergs observed in waters around Labrador by Smith & Donaldson, (1987). These similarities suggest a robust relationship that can be applied to icebergs produced by calving glaciers in other Arctic regions.

The amount of ice per surface area of fjord water decreases in all three fjords between spring and late summer (Figure 6). Decreases in ice coverage could be the result of decreased input from calving glaciers, increases in ice export out of fjords, and/or increased melt of icebergs and sea ice within fjords. We rule out decreased calving fluxes as we observed calving to be steady or increase over the same time period in each fjord (Figure 6). Reductions in sea ice are also unable to account for the observed decrease in ice volume. Analysis of WV images show that the contribution of sea ice to total ice amount decreased by 1.39% between July and late August in SF, and 1.91% per month between mid-July and mid-August in RI. Total ice volumes calculated from L8 images decreased by 10 – 20% over the same timeframe. Increases in export and melting likely both contribute to decreased total iceberg volume. In the winter, sea ice forms in RI and KS as well as outside of all three fjords, effectively blocking export of icebergs from the fjords and leading to a buildup of icebergs which reaches a maximum in the early spring. Break up of sea ice in the late spring and summer allows the buildup of ice to be cleared resulting in a decrease in total ice volume. Additionally, freshwater runoff from the GrIS increases in summer causing stronger net down-fjord flow (Bamber et al., 2012; Polar, 2013; Bartholomaus et al., 2016). Increased runoff may also cause higher rates of iceberg melt, as runoff can take the form of subsurface plumes with positive temperature anomalies that flow down-fjord at depths containing iceberg keels (Carroll et al., 2015; Cowton et al, 2015).

Using standard residence time calculations, we can also obtain first order approximations of ice fluxes using our measurements of total ice volume and tracked iceberg residence times. Using the equation:

$$Ice\ Flux = \frac{Total\ Ice\ Volume}{Ice\ Residence\ Time}$$

and average total ice volumes and residence times for each fjord we estimate ice fluxes of 18, 9.6, and 2.5 $km^3\ yr^{-1}$ for SF, RI, and KS respectively. These estimates compare favorably to measured ice fluxes of 24, 17, and 1.6 $km^3\ yr^{-1}$, and demonstrate that we can obtain reasonable estimates of either ice flux, volume, or residence time if data for the other two properties are available.

Iceberg Classification

While our method is able to quantify many of the icebergs seen in L8 images, we cannot classify all ice for two primary reasons: the difficulty of finding and connecting discrete edges of icebergs within ice mélange, and to a lesser extent the exclusion of very small bits of ice that occupy a single pixel or less of the images.

Ice mélange is most prevalent in SF where a persistent proglacial mélange exists in all available images, typically occupying the majority of the section of fjord running east from the terminus of Helheim Glacier for 20 km. In the images available for this study, we classified between 4.7 and 38.6% of the total ice area in the mélange as icebergs. Despite the fact that our method splits up some large icebergs, we observe a larger average area of icebergs in the ice mélange (3580 m^2) compared with those in the remainder of the fjord (2150 m^2). Icebergs deteriorate through mechanical breakup and melt within fjords, so the largest icebergs will typically be found near parent glaciers that supply them to fjords (Kubat et al., 2007; Enderlin & Hamilton, 2014; Wagner et al.,

2014). Additionally ice mélange has been shown to exert a back-stress sufficient to prevent calving from glacier termini, and similar processes may prevent the breakup of large icebergs in mélange (Amundson et al., 2010).

The volume of icebergs delineated by our automated classification process is on average 76% of the volume delineated manually, and not all ice in ice mélange is classified as part of an iceberg (Figure 2). In the DEMs used for area-volume relationships, ice in mélange that was not part of large icebergs generally had a freeboard height of less than 1 m. We therefore use a total thickness of 10 m for unclassified ice as an upper bound and calculate a volume of ice based on that thickness for unclassified ice in ice mélange. To estimate the volume of ice unaccounted for by the misclassification of large icebergs as smaller icebergs, we assume that the calculated volume of classified icebergs is 76% of the actual volume of those icebergs. Under these assumptions, we estimate that we are able to classify an average of 48% of the total ice mélange volume as icebergs (Table 7). This is likely to be an underestimate, as much of the ice in ice mélange is thin bergy bits and brash ice that has a thickness of less than 10 m.

Table 7: Estimated volumes of ice mélange that was not classified as icebergs in SF.

Date	Total Classified Ice Mélange Volume (km^3)	Volume Missing From Misclassifying Large Icebergs (km^3)	Unclassified Mélange Volume Assuming Average Non-Iceberg Ice Thickness of 10 m (km^3)	Percent of Total Ice Mélange Volume Classified as Icebergs
8/7/2014	1.18	0.38	1.32	41
9/15/2014	3.70	1.19	2.46	50
9/22/14	2.75	0.88	2.31	46
7/7/2015	2.03	0.65	1.27	51
7/16/2015	3.36	1.08	2.57	48

Growlers, bergy bits, and brash ice, collectively defined as pieces of ice smaller than 15 m in length (Canadian Ice Service, 2005), account for a portion of total ice area found using the threshold method that we did not include in our iceberg analyses. The

area of this small ice that was removed ranged from 0.3 – 1.5%, 0.3 – 5.6%, and 0.8 – 3.8% of the total ice area in images from SF, RI, and KS respectively (Table 1). Even if we assume a generous average depth of 10 m for these small bits of ice, the volume of this removed ice is below 1% of the calculated volume of classified icebergs in all images.

Iceberg Distribution

Variability in iceberg size distributions is greater between the three fjords than within any one fjord, suggesting that differences in total ice discharge, calving styles, and grounding line depths account for differences in iceberg properties rather than seasonal effects or geographic features.

The smallest average iceberg size, and therefore the lowest values of the scale and shape parameters for generalized Pareto distributions, were observed in SF (

Table **6,** Figure 13). Calving from Helheim Glacier is dominated by large scale calving events over its entire depth (~600 m) in which buoyant forces lift the terminus, which may be held below flotation by its attachment to the rest of the glacier, and cause icebergs to calve with a bottom out rotation (James et al., 2014; Murray et al., 2015). This calving style causes ice to rise quickly into a tightly packed mélange where collision with other ice is likely. Continued collisions and friction between icebergs transiting the mélange may be responsible for additional breakdown of large icebergs into smaller pieces. Icebergs also move slowly through the mélange, spending more than 70 days there on average, allowing time for melting. The highest water temperatures of the three fjords is observed in SF (ranging from near 0° C near the surface up to 4.5° C at >400 m

depth (Figure 7)), and continued melting of transiting and circulating icebergs may also contribute to the lower average size of icebergs in the fjord (Straneo et al., 2010; Bartholomaus et al., 2016).

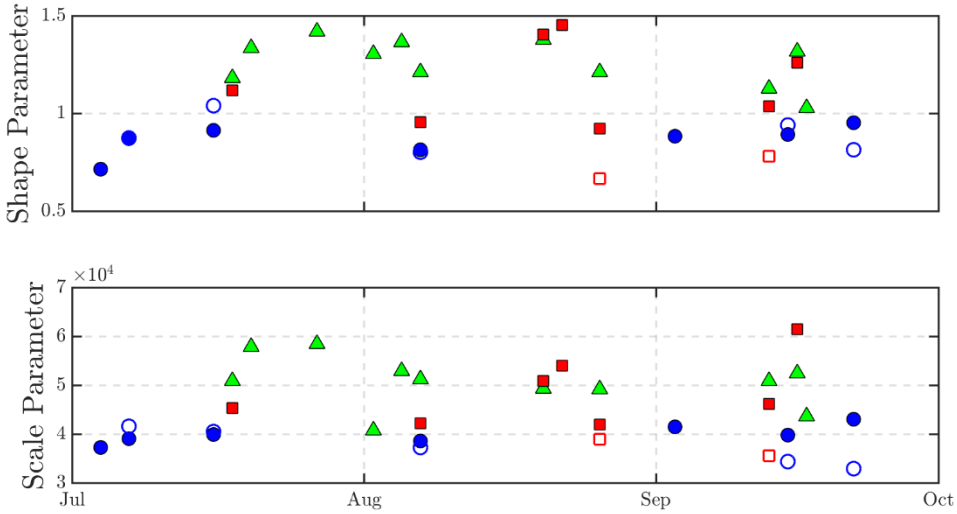

Figure 13: Parameters of generalized Pareto distributions for all images analyzed in SF (blue circles), RI (red squares) and KS (green triangles). Parameters from distributions describing icebergs found using the threshold method are represented by closed symbols, and those using the SFS method are represented by open symbols.

Iceberg mean sizes and parameters of generalized Pareto distributions from RI are intermediate of the three fjords observed (

Table **6**, Figure 13). Additionally, iceberg sizes vary to a greater degree throughout RI than in either SF or KS (Figure 14). Calving of RI occurs by two separate processes: small scale events that occur with high frequency and lead to detachment of non-tabular icebergs, most frequently from crevassed areas of the glacier as weak points in the glacier associated with those crevasses fail; and large scale events in which large tabular icebergs calve from the least crevassed portion of the glacier as buoyant forces act on portions of the glacier that are held below flotation and cause fracturing (Medrzycka et

al., 2016). While the second mechanism is similar to the dominant style of calving in SF, icebergs calved in this manner in RI do not regularly roll as they calve, and generally do not calve into an existing compact ice mélange in summer. Icebergs in RI may therefore be subject to less breakdown via collisions and grinding against other icebergs. We do observe an ephemeral ice mélange in RI when, after a large calving event, a large grouping of ice travels down-fjord staying in close proximity, potentially enhancing breakdown via collision.

In RI, high concentrations of ice occur near the head of the fjord, throughout the north section of the narrow section of the fjord, and behind the sill north of the island (Figure 5). High concentrations to the north may indicate the influence of rotation on surface and subsurface waters flowing down-fjord which is also suggested by the trajectories of tracked icebergs (Figure 12). High ice concentrations to the north of the island are likely the result of larger icebergs reaching depths exceeding the depth of the sill and becoming grounded, as did one of the icebergs that we tracked. Notably, we observed that the temporal variability in iceberg areas decreased with increasing distance from the glacier terminus (Figure 14). We attribute this decrease in variability to the fracture of the largest icebergs as they traverse the fjord which results in more uniform pieces of ice with distance from the glacier terminus.

Total ice coverage in KS is too low to reveal any strong spatial or temporal patterns, but comparisons to RI and SF do reveal interesting contrasts. In KS, variability in iceberg areas, which we approximate using the standard deviation of iceberg areas, is the lowest of the three fjords, and most consistent throughout the fjord (Figure 14). The average iceberg area is largest in KS despite the glacier having the shallowest grounding

line of the three. We attribute the consistency and larger size to a less violent style of calving where ice is not rolling and rising from great depths and therefore remains more intact. The low concentrations of ice also allow less chance of icebergs grinding or knocking together and subsequently breaking into smaller pieces. Water in KS is also colder at equivalent depths than in SF or RI leading to less melting (Figure 7). Finally, though our data are limited, residence times may be lowest of the three fjords in KS, allowing less time for iceberg deterioration during transit through the fjord.

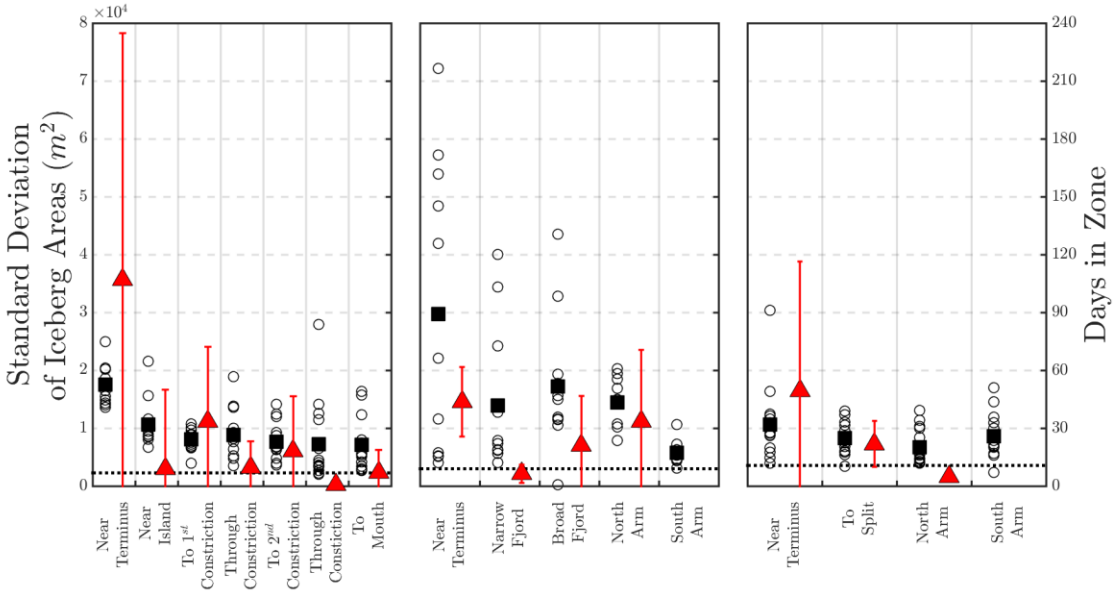

Figure 14: Iceberg size variability and down-fjord speed in geographic zones in SF (left), RI (center), and KS (right). Standard deviation of iceberg areas is displayed for each image (black circles), and the average standard deviation is shown (black squares). Average iceberg area is shown (black dotted line) for reference. Red triangles represent average down-fjord speed of tracked icebergs in each zone. Red error bars are ±1 standard diviation in SF and KS, and represent the range of values in RI where data consists of 2 icebergs only. No tracked icebergs traversed the southern arms of RI or KS, hence no data is presented for iceberg speeds in those zones.

Keel Depths and Melt

Icebergs reaching deeper, warmer fjord waters have the greatest potential to affect water properties because of both their direct contribution of freshwater and their ability to

entrain ambient deep water as the buoyant melt rises upwards through the water column. The melting of icebergs is analogous to the subaqueous melting of glacial termini which has been investigated using observations, numerical modeling, and laboratory experiments (Eijpen et al., 2003; Rignot et al., 2010; Xu et al., 2012).

We calculated the total surface area of icebergs at different depths based on block shaped icebergs. This approach may overestimate surface area as real icebergs are likely to have a shape that tapers with depth rather than maintaining a constant horizontal cross section. Our estimates of submerged surface area of icebergs exceeds that of the glacier faces throughout all three fjords (

Table **8**).

Icebergs have the greatest potential to influence water properties in SF because of the high concentration of icebergs and relatively high water temperature. Water temperature in SF increases below the surface layer, reaching temperatures of 2°C at 200m and rising to 3.5°C at 400m (Figure 7) (Sutherland et al. 2014). Enderlin & Hamilton (2014) calculated an average iceberg melt rate of ~0.39 m d^{-1} in SF. Applying that melt rate to the total surface area of submerged icebergs in SF yields a freshwater contribution from iceberg melt of 0.083 km^3 d^{-1} to the fjord. This melt rate may be an upper bound on summer melt, but is unrealistic as a year round estimate as it would imply a total freshwater input from iceberg melt of 30 km^3 yr^{-1}, which is higher than our measured annual ice flux of 24 km^3 yr^{-1}. The discrepancy may in part be due to small icebergs which likely experience less overall melt, as their keels remain in the upper portion of the water column where temperatures are low. Applying the average melt rate to only the surface area of icebergs below 100 m, where water temperatures begin to

increase, yields a freshwater input from iceberg melt of 0.009 km^3 d^{-1}, which could be considered a lower bound on freshwater input from iceberg melt. This is still greater than the 0.006 km^3 d^{-1} of freshwater from melting of the glacier face, based on a submarine melt rate of 1.78 m d^{-1} derived by Sutherland & Straneo (2012), though the input of freshwater from iceberg melt is distributed throughout the fjord rather than concentrated in one spot as is the input from submarine glacial melt.

Table 8: Water temperature and average surface area (km^2) of ice at depth. Temperatures are averages of measurements taken throughout each fjord over three summers. Iceberg areas assume that icebergs maintain their cross-sectional area at the water line throughout their depths.

	Depth (m)	0-100	100-200	200-300	300-400	400+
SF	Mean Temp. (°C)	1.03	1.91	2.93	3.62	3.95
	Glacier Face	0.55	0.55	0.55	0.55	1.1
	Icebergs	188	21.9	2.86	0	0
RI	Mean Temp. (°C)	1.41	1.84	2.07	2.28	2.75
	Glacier Face	0.47	0.47	0.47	0.47	2.1
	Icebergs	34.1	5.90	1.20	0.14	0
KS	Mean Temp. (°C)	0.62	1.07	1.89	-	-
	Glacier Face	0.42	0.42	0.21	-	-
	Icebergs	6.29	1.28	0	-	-

CHAPTER V

CONCLUSIONS

Icebergs are a significant component of total freshwater discharge from the GrIS. We are able to use available satellite data to quantify distributions of iceberg sizes and total coverage of fjords by icebergs. Additionally, by using high resolution satellite imagery to construct DEM's we created a robust relationship between iceberg areas and volumes, and used that relationship to quantify the total volume of ice present in fjords and to estimate iceberg keel depths and subsurface iceberg surface area.

We found substantial differences in iceberg characteristics between the three fjords that we investigated. Differences in icebergs are tied to differences in glacier grounding line depths, calving styles, and fjord water properties and circulation. We determined that iceberg size distributions follow generalized Pareto distributions, and we recommend using Pareto laws when determining iceberg size distributions to seed models.

This work represents first steps towards quantifying iceberg properties on a large scale and quantifying freshwater input from iceberg melt. Future study includes applying these methods to other fjords, exploring the use of radar rather than optical satellite observations to obtain year-round coverage, using these distributions to seed icebergs in numerical ocean models, and refining estimates of iceberg keel depths, subaqueous surface areas, and freshwater input from iceberg melt. This work highlights the need for more observations of iceberg keel shapes and depths. Expanding records of surface

currents through continued use of icebergs as drifters or other means, as well as obtaining measurements of water properties and circulation within other fjords is also necessary to continue and expand this work.

REFERENCES CITED

Amundson, J. M., Fahnestock, M., Truffer, M., Brown, J., Lüthi, M. P., & Motyka, R. J. (2010). Ice mélange dynamics and implications for terminus stability, Jakobshavn Isbrse, Greenland. *Journal of Geophysical Research: Earth Surface*, *115*(1), 1–12. http://doi.org/10.1029/2009JF001405

Andres, M., Silvano, A., Straneo, F., & Watts, D. R. (2015). Icebergs and Sea Ice Detected with Inverted Echo Sounders. *Journal of Atmospheric and Oceanic Technology*, *32*(5), 1042–1057. http://doi.org/10.1175/JTECH-D-14-00161.1

Azetsu-Scott, K., & Syvitski, J. P. M. (1999). Influence of melting icebergs on distribution, characteristics and transport of marine particles in an East Greenland fjord. *Journal of Geophysical Research*, *104*(C3), 5321. http://doi.org/10.1029/1998JC900083

Bamber, J., Broeke, M. Van Den, Ettema, J., Lenaerts, J., & Rignot, E. (2012). Recent large increases in freshwater fluxes from Greenland into the North Atlantic. *Geophysical Research Letters*, *39*, 8–11. http://doi.org/10.1029/2012GL052552

Barker, A., Sayed, M., & Carrieres, T. (2004). Determination of Iceberg Draft , Mass and Cross- Sectional Areas NRC Publications Archive (NPArC). *Proceedings of The Fourteenth International Offshore and Polar Engineering Conference*, (January).

Bartholomaus, T. C., Stearns, L. A., Sutherland, D. A., Shroyer, E. L., Nash, J. D., Walker, R., … Broeke, M. Van Den. (2016). Contrasts in the response of adjacent fjords and glaciers to ice-sheet surface melt in West Greenland. *Annals of Glaciology*. http://doi.org/10.1017/aog.2016.19

Bigg, G. R., & Nicholls, K. W. (2001). Iceberg trajectory modeling and meltwater injection. *Journal of Geophysical Research*, *106*(C9), 19903 – 19915.

Bigg, G. R., Wadley, M. R., Stevens, D. P., & Johnson, J. A. (1997). Modelling the dynamics and thermodynamics of icebergs. *Cold Regions Science and Technology*, *26*, 113–135.

Bigg, G. R., & Wilton, J. (2013). Iceberg risk in the Titanic year of 1912 : was it exceptional? *Weather*, *69*(4), 100 – 104.

Box, J., & Colgan, W. (2013). Greenland Ice Sheet Mass Balance Reconstruction . Part III : Marine Ice Loss and Total Mass Balance (1840 – 2010). *Journal of Climate*, *26*, 6990–7002. http://doi.org/10.1175/JCLI-D-12-00546.1

Canadian Ice Service. (2005). *Manual of Standard Proceedures for Observing and Reporting Ice Conditions*. (D. Fequet, Ed.) (Revised 9t). Ottawa, Ontario: Environment Canada.

Carroll, D., Sutherland, D. A., Shroyer, E. L., Nash, J. D., Catania, G. A., & Stearns, L. A. (2015). Modeling Turbulent Subglacial Meltwater Plumes : Implications for Fjord-Scale Buoyancy-Driven Circulation. *Journal of Physical Oceanography*, *45*, 2169–2185. http://doi.org/10.1175/JPO-D-15-0033.1

Cowton, T., Slater, D., Sole, A., Goldberg, D., & Niewnow, P. (2015). Modeling the impact of glacial runoff on fjord circulation and submarine melt rate using a new subgrid-scale parameterisization for glacial plumes. *Journal of Geophysical Research: Oceans*, *120*, 796–812. http://doi.org/10.1002/2014JC010324.Received

Crocker, G. B. (1993). Size distributions of bergy bits and growlers calved from deteriorating icebergs. *Cold Regions Science and Technology*, *22*, 113–119.

Death, R., Siegert, M. J., Bigg, G. R., & Wadley, M. R. (2006). Modelling iceberg trajectories , sedimentation rates and meltwater input to the ocean from the Eurasian Ice Sheet at the Last Glacial Maximum. *Palaeogography, Palaeoclimatology, Palaeoecology*, *236*, 135–150. http://doi.org/10.1016/j.palaeo.2005.11.040

Dowdeswell, J. A., & Dowdeswell, E. K. (1989). Debris in Icebergs and Rates of Glaci-Marine Sedimentation : Observations from Spitsbergen and a Simple Model. *The Journal of Geology*, *97*(2), 221–231.

Dowdeswell, J. A., & Forsberg, C. F. (1992). The size and frequency of icebergs and bergy bits derived from tidewater glaciers in Kongsfjorden , northwest Spitsbergen. *Polar Research*, *11*(2), 81–91.

Eijpen, K. J., Warren, C. R., & Benn, D. I. (2003). Subaqueous melt rates at calving termini : a laboratory approach. *Annals of Glaciology*, *36*, 179 – 183.

Enderlin, E. M., & Hamilton, G. S. (2014). Estimates of iceberg submarine melting from high-resolution digital elevation models: application to Sermilik Fjord, East Greenland. *Journal of Glaciology*, *60*(224), 1084–1092. http://doi.org/10.3189/2014JoG14J085

Enderlin, E. M., Howat, I. M., Jeong, S., Noh, M.-J., van Angelen, J. H., & van den Broeke, M. R. (2014). An improved mass budget for the Greenland ice sheet. *Geophysical Research Letters*, *41*, 866–872. http://doi.org/10.1002/2013GL059010.Received

Fichefet, T., Poncin, C., Goosse, H., Huybrechts, P., Janssens, I., & Le Treut, H. (2003). Implications of changes in freshwater flux from the Greenland ice sheet for the climate of the 21st century. *Geophysical Research Letters*, *30*(17), 1911–1915. http://doi.org/10.1029/2003GL017826

Foga, S., Stearns, L. A., & van der Veen, C. J. (2014). Using satellite remote sensing data to determine terminus and ice melange variability at Helheim Glacier, East Greenland. *Marine Technology Society Journal (Polar Instruments and Methods)*. http://doi.org/10.4013/MTSJ.48.5.3

Grobe, B. H. (1987). A Simple Method for the Determination of Ice-Rafted Debris in Sediment Cores. *Polargorschung*, *57*(3), 123–126.

Hotzel, I. S., & Miller, J. D. (1983). ICEBERGS : THEIR PHYSICAL DIMENSIONS AND THE PRESENTATION AND APPLICATION OF. *Annals of Glaciology*, *4*, 116–123.

Huang, X., Zhang, L., & Li, P. (2007). Classification and Extraction of Spatial Features in Urban Areas Using High-Resolution Multispectral Imagery. *IEEE Geoscience and Remote Sensing Letters*, *4*(2), 260–264.

James, T. D., Murray, T., Selmes, N., Scharrer, K., & Leary, M. O. (2014). Buoyant flexure and basal crevassing in dynamic mass loss at Helheim Glacier. *Nature Geoscience*, *7*, 593–596. http://doi.org/10.1038/NGEO2204

Joughin, I., Howat, I. M., Smith, B., & Scambos, T. (2011). *MEaSUREs Greenland Ice Velocity: Selected Glacier Site Velocity Maps from InSAR, Version 1*. Boulder, CO USA.

Joughin, I., Smith, B., Howat, I. M., Scambos, T., & Moon, T. (2010). Greenland Flow Variability from Ice-Sheet-Wide Velocity Mapping. *Journal of Glaciology*, *56*, 415–430. http://doi.org/http://dx.doi.org/10.3189/002214310792447734

Kubat, I., Sayed, M., Savage, S. B., Carrieres, T., & Crocker, G. B. (2007). An Operational Iceberg Deterioration Model. *Proceedings of the Seventeenth International Offshore and Polar Engineering Conference*, 652–657.

Larsen, P., Overgaard Hansen, M., Buus-hinkler, J., Krane, K. H., & Sønderskov, C. (2015). Field tracking (GPS) of ten icebergs in eastern Baffin Bay , offshore Upernavik , northwest Greenland. *Journal of Glaciology*, *61*(227), 421–437. http://doi.org/10.3189/2015JoG14J216

Levine, R. C., & Bigg, G. R. (2008). Sensitivity of the glacial ocean to Heinrich events from different iceberg sources , as modeled by a coupled atmosphere-iceberg-ocean model. *Paleoceanography*, *23*, 1–16. http://doi.org/10.1029/2008PA001613

Martin, T., & Adcroft, a. (2010). Parameterizing the fresh-water flux from land ice to ocean with interactive icebergs in a coupled climate model. *Ocean Modelling*, *34*(3-4), 111–124. http://doi.org/10.1016/j.ocemod.2010.05.001

Medrzycka, D., Benn, D. I., Box, J. E., Copland, L., Balog, J., Medrzycka, D., … Balog, J. (2016). Calving behavior at Rink Isbræ , West Greenland , from time-lapse photos. *Arctic, Antarctic, and Alpine Research*, *48*(2), 263–277.

Moon, T., Joughin, I., Smith, B., & Howat, I. (2012). 21st-Century Evolution of Greenland Outlet Glacier Velocities. *Science*, *336*, 576–579.

Moratto, S. Z. M., Broxton, M. J., Beyer, R. A., Lundy, M., & Husmann, K. (2010). Ames Stereo Pipeline , NASA ' s Open Source Automated Stereogrammetry, 1–2.

Mugford, R. I., & Dowdeswell, J. A. (2010). Modeling iceberg rafted sedimentation in high latitude fjord environments. *Journal of Geophysical Research*, *115*(March), 1–21. http://doi.org/10.1029/2009JF001564

Murray, T., Selmes, N., James, T. D., Edwards, S., Martin, I., Timothy, O., … Baugé, T. (2015). Dynamics of glacier calving at the ungrounded margin of Helheim Glacier, southeast Greenland. *Journal of Geophysical Research : Earth Surface*, *120*, 964–982. http://doi.org/10.1002/2015JF003531.Received

Neshyba, S. (1980). On the size distribution of Antarctic icebergs. *Cold Regions Science and Technology*, *1*, 241–248.

Noh, M.-J., & Howat, I. M. (2015). Automated stereo-photogrammetric DEM generation at high latitudes: Surface Extraction with TIN-based Search-space Minimization (SETSM) validation and demonstration over glaciated regions. *GIScience & Remote Sensing*, *52*(2), 198–217. http://doi.org/10.1080/15481603.2015.1008621

Raiswell, R., Tranter, M., Benning, L. G., Siegert, M., De, R., Huybrechts, P., & Payne, T. (2006). Contributions from glacially derived sediment to the global iron (oxyhydr) oxide cycle : Implications for iron delivery to the oceans. *Geochimica et Cosmochimica Acta*, *70*, 2765–2780. http://doi.org/10.1016/j.gca.2005.12.027

Rignot, E., Fenty, I., Xu, Y., Cai, C., Velicogna, I., Cofaigh, C. Ó., … Duncan, D. (2016). Bathymetry data reveal glaciers vulnerable to ice-ocean interaction in Uummannaq and Vaigat glacial fjords , west Greenland. *Geophysical Research Letters*, *43*, 2667–2674. http://doi.org/10.1002/2016GL067832.Received

Rignot, E., Koppes, M., & Velicogna, I. (2010). Rapid submarine melting of the calving faces of West Greenland glaciers. *Nature Geoscience*, *3*(3), 187–191. http://doi.org/10.1038/ngeo765

Robe, R. Q. (1980). Iceberg Drift and Deterioration. In S. C. Colbeck (Ed.), *Dynamics of Snow and Ice Masses* (pp. 211 – 259). New York, NY: Academic Press, INC.

Rosenau, R., Scheinert, M., & Dietrich, R. (2015). A processing system to monitor Greenland outlet glacier velocity variations at decadal and seasonal time scales utilizing the Landsat imagery. *Remote Sensing of the Environment*, *169*, 1–19.

Savage, S. B., Crocker, G. B., Sayed, M., & Carrieres, T. (2000). Size distributions of small ice pieces calved from icebergs. *Cold Regions Science and Technology*, *31*, 163–172.

Smith, S. D., & Donaldson, N. R. (1987). Dynamic modelling of iceberg drift using current profiles. *Canadian Technical Report of Hydrography and Ocean Sciences*, (91).

Stouffer, R. J., Yin, J., Gregory, J. M., Dixon, K. W., Spelman, M. J., Hurlin, W., … Weber, S. L. (2006). Investigating the Causes of the Response of the Thermohaline Circulation to Past and Future Climate Changes. *Journal of Climate*, *19*(8), 1365–1387. http://doi.org/10.1175/JCLI3689.1

Straneo, F., Hamilton, G. S., Sutherland, D. A., Stearns, L. A., Davidson, F., Hammill, M. O., … Rosing-asvid, A. (2010). Rapid circulation of warm subtropical waters in a major glacial fjord in East Greenland. *Nature Geoscience*, *3*(3), 182–186. http://doi.org/10.1038/ngeo764

Sutherland, D. A., Roth, G. E., Hamilton, G. S., Mernild, S. H., Stearns, L. A., & Straneo, F. (2014). Quantifying flow regimes in a Greenland glacial fjord using iceberg drifters. *Geophysical Research Letters*, *41*(23), 8411–8420.

Sutherland, D. A., & Straneo, F. (2012). Estimating ocean heat transports and submarine melt rates in Sermilik Fjord , Greenland , using lowered acoustic Doppler current profiler (LADCP) velocity profiles. *Annals of Glaciology*, *53*(60), 50–58. http://doi.org/10.3189/2012AoG60A050

Sutherland, D. A., Straneo, F., & Pickart, R. S. (2014). Characteristics and dynamics of twomajor Greenland glacial fjords. *Journal of Geophysical Research: Oceans*, *119*, 3767–3791. http://doi.org/10.1002/2013JC009786.Received

Syvitski, J. P. M., Andrews, J. T., & Dowdeswell, J. A. (1996). Sediment deposition in an iceberg-dominated glacimarine environment , East Greenland : basin fill implications. *Global and Planetary Change*, *12*, 251–270.

Tournadre, J., Bouhier, N., Girard-Ardhuin, F., & Rémy, F. (2016). Antarctic icebergs distributions 1992-2014. *Journal of Geophysical Research: Oceans*, *121*, 327–349. http://doi.org/10.1002/2015JC011178

Tournadre, J., Girard-Ardhuin, F., & Legrésy, B. (2012). Antarctic icebergs distributions, 2002-2010. *Journal of Geophysical Research: Oceans*, *117*(5), 2002–2010. http://doi.org/10.1029/2011JC007441

USGS. (2016). *Lansat 8 (L8) Data Users Handbook*. U.S. Geological Survey.

van den Broeke, M., Bamber, J., Ettema, J., Rignot, E., Schrama, E., Berg, W. J. Van De, … Wouters, B. (2009). Partitioning Recent Greenland Mass Loss. *Science*, *326*, 984–986. http://doi.org/10.1126/science.1178176

Velicogna, I., Sutterley, T. C., & Broeke, M. R. Van Den. (2014). Regional acceleration in ice mass loss from Greenland and Antarctica using GRACE time-variable gravity data. *Geophysical Research Letters*, *41*, 8130–8137. http://doi.org/10.1002/2014GL061052.Received

Wadhams, P. (1988). Winter Observations of Iceberg Frequencies and Sizes in the South. *Journal of Geophysical Research*, *93*(C4), 3583–3590.

Wagner, T. J. W., Wadhams, P., Bates, R., Elosegui, P., Stern, A., Vella, D., … Nicholls, K. W. (2014). The " footloose " mechanism : Iceberg decay from hydrostatic stresses. *Geophysical Research Letters, 41*, 5522–5529. http://doi.org/10.1002/2014GL060832.We

Williams, R., & Macdonald, M. (1995). An image segmentation technique to infer the outlines of icebergs, depicted in satellite images, from their shadows and bright sunlit surfaces. *Proceedings of the Third Australian and New Zealand Conference on Intelligent Information Systems*, 76–81.

Xu, Y., Rignot, E., Menemenlis, D., & Koppes, M. (2012). Numerical experiments on subaqueous melting of Greenland tidewater glaciers in response to ocean warming and enhanced subglacial discharge. *Annals of Glaciology*, *53*(60), 229–234. http://doi.org/10.3189/2012AoG60A139

Yang, Q., Dixon, T. H., Myers, P. G., Bonin, J., Chambers, D., & Broeke, M. R. Van Den. (2016). Labrador Sea convection and Atlantic overturning circulation. *Nature Communications*, *7*, 1–7. http://doi.org/10.1038/ncomms10525